

# Modelling Emission from Dust in Dual-Chemistry post-AGB Stars

João Fernando Ciotta Neves

MSc by Research  
Centre for Astrophysics Research  
Faculty Engineering & Information Sciences  
University of Hertfordshire, U.K.

## Abstract

Post-AGB (post-asymptotic giant branch) stars are luminous stars of low and intermediate initial mass ( $M_* \leq 9M_\odot$ ) in a final stage of evolution towards becoming white dwarfs. These stars are surrounded by envelopes of gas and dust expelled at the end of the AGB (asymptotic giant branch) phase. The circumstellar dust chemistry is expected to be either oxygen or carbon dominated, depending on the chemistry of the star at the end of the AGB phase. Recent observations have revealed a surprising range number of carbon-rich stars with a range of sharp crystalline silicate features in their spectra, typical of a complex oxygen-rich chemistry. These dual-chemistry objects are something of a puzzle, but it is possible to gain important knowledge about these objects by investigating the structure and density of circumstellar envelopes using realistic computer models of these systems. The aim of this project is to develop realistic models of the dust emission from post-AGB stars using a sophisticated radiative transport code. Firstly, a detailed study of two radiative equilibrium codes is developed with focus on the differences between two methods of solving the radiative transfer problem: the classic ray-tracing method (DART) and the monte-carlo method (CSRE); and on the modifications made that enable CSRE to model post-AGB stars. CSRE has some advantages comparing with DART. In particular it returns physically correct results for systems with high densities. Secondly, CSRE model calculations are used to investigate the Red Rectangle. Two alternative models are discussed, one based on a simple density distribution using small dust grains and the other on a more complicated distribution of large grains, proposed by Men'shchikov et al. (2002). We concluded that this proposed model may be too simplistic in its treatment of the scattering and dust properties, as the need of a complex density distribution of large grains is not clear from our CSRE model results, in fact, a model using exclusively standard size grains in a simple density distribution is equally consistent with the observations.

## Resumo

Estrelas de tipo post-AGB (post-asymptotic giant branch) são estrelas luminosas com baixa ou intermédia massa inicial ( $M_* \leq 9M_\odot$ ) na fase final da sua evolução em direcção à fase de Anãs brancas. Estas estrelas têm envelopes de gás e poeiras libertados no fim da fase AGB. A composição química das

poeiras circum-estelares pode, em princípio, ter um de dois elementos químicos dominantes: oxigénio ou carbono, dependendo da composição química da estrela no fim da fase AGB. Observações recentes revelam um inesperado número de estrelas com propriedades duplas, i.e. estrelas com elementos resultantes da coexistência de oxigénio e carbono. Estes objectos são um puzzle, mas é possível descobrir importantes informações sobre estas estrelas desenvolvendo e usando modelos computacionais destes sistemas. O objectivo deste projecto é desenvolver e testar modelos realísticos da emissão electromagnética do material que envolve (gás e poeiras) estas estrelas.

## 1 - Introduction

Post-AGB (post-asymptotic giant branch) stars are luminous stars of low and intermediate initial mass ( $M_* \leq 9M_\odot$ ) in a final stage of evolution towards becoming white dwarfs. They are surrounded by expanding envelopes of gas and dust, expelled at the end of the AGB phase, which is characterised by very strong mass loss,  $10^{-7} - 10^{-4} M_\odot \text{ yr}^{-1}$ . The circumstellar dust chemistry is expected to be either oxygen or carbon dominated, depending on the chemistry of the star at the end of the AGB phase. The recent ISO (Infrared Space Observatory) mission revealed a range of sharp crystalline features in the spectra of many evolved objects, suggesting a complex oxygen-rich (O-rich) chemistry. While some of these objects have O-rich exciting stars, as expected, a surprising number have carbon-rich (C-rich) stars, as well as strong PAH (polycyclic aromatic hydrocarbon) dust features.

These dual-chemistry objects are something of a puzzle, but are thought to arise from interaction of the AGB star with a binary companion, resulting in the formation of a stable circumstellar disc (e.g. Waters et al., 1998). This disc is able to trap O-rich material which survives during the transition of the star into a C-rich phase. An alternative hypothesis is that the O-rich material lies at greater distances from the exciting star and results from the disruption of an Oort cloud of cometary bodies (Cohen et al., 1999).

Modelling the radiative transfer problem in these complex objects requires a sophisticated radiation transport code, that is

different locations in the circumstellar envelope, and very dense regions (e.g. discs) in the innermost regions of the system. This dissertation investigates the radiative transport in the material distribution in the circumstellar dust shells with emphasis on the dust grains.

## 2 - Post-Main sequence stellar evolution

The Post-Main Sequence evolution of stars with initial mass in the range of  $0.8M_\odot \leq M_{*}^{\text{init}} \leq 9M_\odot$  is: Red Giant Branch, Horizontal Branch, Asymptotic Giant Branch, Protoplanetary Nebulae, Planetary Nebulae, and White Dwarf. This mass range arises because, for  $M_{*}^{\text{init}} \geq 0.8M_\odot$  the star can sustain hydrogen burning and evolve to the AGB phase, and for  $M_{*}^{\text{init}} \leq 9M_\odot$  the star will not end as a supernova as its degenerate core will not exceed the Chandrasekhar mass limit of  $\sim 1.4M_\odot$ .

Post-Main sequence evolution for low and intermediate mass stars begins when there is no more hydrogen in the stellar core and shell hydrogen burning starts. At this point the star ascends in the HR diagram to the Red Giant Branch. The star becomes a giant as the hydrogen burns in the envelope. The ignition of this hydrogen causes it to expand and the core contracts.

The envelope is convective and causes the new nuclear processed material generated in the core to be dredged-up<sup>1</sup>. This is the first dredge-up episode and mixes the products of hydrogen burning to the stellar surface.

Low-mass stars,  $\leq 2M_\odot$ , develop an electron-degenerate helium core during the RGB. If the helium core reaches  $\sim 0.45M_\odot$ , a helium flash occurs until degeneracy is removed and normal helium burning begins. This terminates the ascent on the giant branch.

Intermediate-mass stars can initiate core He burning in non degenerate conditions, so the He flash does not occur. Then a phase of core helium burning with a hydrogen-burning shell occurs.

At this point the star finds itself on the Horizontal Branch in the HR diagram. This horizontal strip of stars in the diagram is populated by stars bluer and fainter than those on the red giant branch. These stars are thought to be burning He in their core and H in a surrounding shell. The horizontal branch is a stage of stellar evolution which follows the red giant branch and precedes the Asymptotic Giant Branch phase, however the path to the horizontal branch may include several oscillations back

powered the horizontal branch stops due the exhaustion of He in the core, the carbon/oxygen core is then surrounded by two shells, a helium and a hydrogen shell.

Both low and intermediate mass stars develop an electron-degenerate carbon/oxygen core after core He exhaustion. This is the beginning of the AGB phase.

## 2.1 Asymptotic Giant Branch phase

The term asymptotic is used because the evolution of a star in the HR diagram, during this phase, approaches the RGB. The AGB can be divided into two phases: 1) the early AGB (E-AGB), and the 2) the thermal-pulsing AGB (TP-AGB). During the E-AGB phase<sup>2</sup>, hydrogen shell burning has stopped and the luminosity of the star is provided by He shell burning. In this phase, both the stellar luminosity and the temperature vary. The luminosity increases and the temperature decreases. When a critical value of the luminosity is reached, H begins to burn again in a thin shell. This is the end of the E-AGB and the beginning of the TP-AGB phase.

Depending on the core mass, the lifetime of the early AGB phase is  $\sim 10^7$  yr. During most of the time (90%) in the TP-AGB phase, hydrogen shell burning is the chief source of energy. However, the mass of the He shell below the H shell increases and this will cause a thermonuclear runaway. This takes place when helium ignites and causes the star to expand. This He-flash or thermal pulse lasts until the He shell burning ceases due to its expansion and cooling. As in the proto-stellar phase, the gravity plays its role. The material falls towards the centre, the density and temperature increase and the star returns to a steady state of hydrogen shell burning. The mass of the helium shell will increase again and another thermal pulse starts. The number of thermal pulses that a star suffers depends on its mass.

After each flash, the bottom of the convective envelope reaches down past the hydrogen/helium surface of separation and a third dredge-up occurs. As result of these dredge-up episodes, the photospheric chemical composition of AGB stars is changed. The formation of C-rich stars is a consequence of the third dredge-up. The amount of mass that is dredged-up is  $\sim 6 \times 10^{-3} M_{\odot}$  for a core mass of  $0.6 M_{\odot}$  (for a recent review on

stellar evolution during the AGB phase, Herwig, 2005). This thermal pulse repeats every  $10^4$  to  $10^5$  yr depending on the

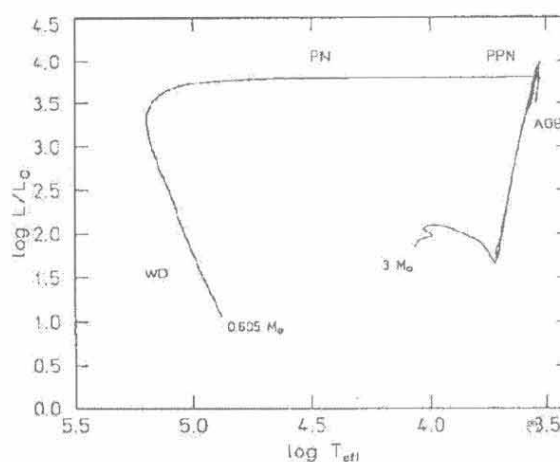


Figure 2.1: Hertzsprung-Russell diagram of a complete  $3 M_{\odot}$  post main sequence evolution track for solar metallicity. The thermal pulses described in the text, at the end of the AGB phase, are visible. The final mass is  $0.605 M_{\odot}$ . (Adapted from Blöcker, 2001).

## 2.2 O-rich or C-rich

AGB stars can be roughly classified as either oxygen or carbon rich based on the abundance ratio of carbon (C) and oxygen (O) in their photospheres.

The ratio C/O is the single most important characteristic of the star that will decide its chemical evolution from the AGB, through to the post-AGB phase and PN.

As the evolution from O-rich to C-rich takes place on the AGB phase, the dust surrounding post-AGB stars and PNe should be either O-rich or C-rich with a central star of similar chemical composition.

Why? Because the CO molecule is stable. The atoms of the less abundant element (whether O or C) are tied up in CO molecules and are unavailable to form other molecules. The excess of the more abundant element is free to form other molecular species.

In an O-rich star the excess in oxygen can be used to form molecules in the

photosphere such as OH, H<sub>2</sub>O, CO<sub>2</sub>, SiO (Waters, 2004). The spectrum of a C-rich star has bands of C<sub>2</sub>H<sub>2</sub>, C<sub>2</sub>, and HCN. A

<sup>2</sup> Dredge-up is the convective mixing process that brings material processed by nucleosynthesis to the surface, where it can be observed and will be ejected into the circumstellar envelope through wind mass loss.

band usual attributed to the mineral SiC is also seen as a dust feature in these stars. This chemical balance will be reflected in the composition of the dust that forms around the star.

For AGB stars where photospheres are obscured by circumstellar dust, it is possible to study their chemical nature using infrared spectroscopy of the circumstellar envelope.

### 2.3 Mass loss during the AGB

AGB stars have low surface gravity and a small escape velocity due to a small mass and large radius. Under these conditions, the outer layers of the star can become unstable. The unstable surface material falls back into the star and, as this process is repeated, surface pulsations sets in. These pulsations can be the cause for mass loss in the AGB phase (Bowen, 1988).

These accelerated layers move away from the star. Material with high densities and low temperature can be found at several stellar radii. Dust is formed under these conditions.

Dust has high opacities at near-IR and optical wavelengths and absorbs stellar radiation and momentum. The dust grains are important in driving the wind (gas and dust) because they transfer momentum from the radiation field to the gas through gas-grain collisions. This momentum is gained by the dust grains in the first place, because the stellar photons flow predominantly in the outward radial direction, but the re-radiated (at IR wavelengths) photons escape from the dust grains almost isotropically. This dust-driven wind (Kwok, 1975, 2000; Netzer & Elitzur, 1993; Tielens, 1983) is responsible for the AGB mass-loss at the rate of  $\sim 10^{-7}$  to  $10^{-5} M_{\odot} \text{ yr}^{-1}$  (e.g. Kwok, 2000; Ueta, 2002).

At the same time, the thermal pulsations continue. The mass of the hydrogen rich shell is being reduced as the region where the hydrogen is being consumed expands radially and the mass loss continues to remove the material from the surface. When the mass of the hydrogen envelope is reduced below a critical value ( $M \sim 10^{-3} M_{\odot}$ , Schönberner, 1983) the mass loss rate decreases sharply, from  $\sim 10^{-4} M_{\odot} \text{ yr}^{-1}$  at the end of the AGB, to  $\sim 10^{-7} M_{\odot} \text{ yr}^{-1}$  in the post-AGB phase (Blöcker, 1995a). At this point, the circumstellar envelope detaches from the central star, the star begins its evolutionary journey to higher temperatures in the HR diagram (PPN label in the figure 2.1).

This is the end of the AGB phase and the beginning of the post-AGB phase (or PPN).

### 2.4 Post-AGB phase

The Post-AGB phase begins with the end of the large scale mass loss in the final stages of the AGB phase and ends when the central star is hot enough ( $T_{\text{e}} \sim 30,000\text{K}$ ) to ionise the circumstellar material. The typical time scales depend greatly on the core mass. This transition time ranges from extremely short for the most massive objects ( $M \sim 7 M_{\odot}$ ),  $\sim 30$  yr, to  $\sim 10^3$  yr for the less massive stars (Blöcker, 1995b). For the most massive objects, it is possible to observe stellar evolution in real time (Engels, 2005; Van Winckel, 2003).

These time scales result from numerical models for the evolution of post-AGB stars (e.g., Blöcker, 1995b; Vassiliadis & Wood, 1994) which rely crucially on the core mass-luminosity ( $M_{\text{c}} - L$ ) relation. The  $M_{\text{c}} - L$  relation, discovered by Paczynski (1970) as a result of numerical computations of stellar evolution models, states that the relationship between the luminosity ( $L$ ) and the core mass of the object ( $M_{\text{c}}$ ) is (almost) linear.

A typical post-AGB star has luminosity of  $\sim 10^3$  to  $10^4 L_{\odot}$  (for a recent review, Van Winckel, 2003) and the estimated transition times are inversely proportional to the core mass (Blöcker, 1995b), therefore a different expression for the  $M_{\text{c}} - L$  relation will result in different values for the transition times.

However, our understanding of these systems is still incomplete and additional physical processes can play an important role in defining the pace of the post-AGB evolution, e.g. Zijlstra et al. (2001) argue that the lifetime of some post-AGB stars can have values of the order of  $10^4$  years. This is due to accretion from a circumstellar disc (or torus). This non-expanding gas near the star and its accretion by the central star adds gas to compensate the mass lost from nuclear burning and mass loss, thus the evolution to higher temperatures would be delayed.

Post-AGB stars are relatively rare because this is a fast evolutionary phase as the fraction of time spent in the post-AGB phase is  $\sim 10\%$  of the time spent in the PN phase (Kwok, 2000).

As a more evolved object compared with the AGB phase, the detached dust shells of the post-AGB star can be observed (due to their larger spatial extent) and their spectra reveal a O-rich or a C-rich chemistry. In figures 2.2 and 2.3 adapted from Garcia-Lario & Calderon (2003), an evolutionary sequence is proposed for O-rich and C-rich, ranging from AGB to PNe. They used the ISO spectra in the Data Archive to build a sample of 330 sources containing both O-rich stars (70%) and C-rich stars (23%). See next section to find out about the missing 7%!

Figures 2.2 and 2.3 can be interpreted as evidence for increasing mass loss rate, increasing thickness of the circumstellar shell, gradual cooling of the circumstellar material when the star enters the post-AGB phase and changing properties in

the dust grains. This is in good agreement with the theory of stellar evolution.

For the O-rich sequence (figure 2.2), the silicate emission bands at  $9.7$  and  $18\ \mu\text{m}$  are increasing in strength with evidence of increasing mass loss rate. Crystalline dust features start to appear in the lower spectra. This is evidence of a change in dust properties, from amorphous to crystalline.

For the C-rich sequence (figure 2.3), the silicon carbide mineral (SiC) emission band at  $11.3\ \mu\text{m}$  is increasing in strength which is also evidence of a change in dust properties, from aliphatic to aromatic.

In both O- and C-rich sequences, dust features can turn from emission to absorption and this results from an increase in optical depth in the envelope as the thickness of the circumstellar shell increases. Also, the circumstellar envelope is cooling as the peak of the infrared emission is shifting towards longer wavelengths.

In O-rich post-AGB stars the silicates dominate with a broad feature at  $9.7\ \mu\text{m}$  and  $18\ \mu\text{m}$ . At longer wavelengths, crystalline silicates were identified in these stars, e.g. olivines ( $\text{Mg}_2\text{SiO}_4$ ) and pyroxenes ( $\text{MgSiO}_3$ ) and also strong additional features and complexes at  $23.5$ ,  $27.5$ ,  $33.5$ ,  $40.8\ \mu\text{m}$ , and  $60.0\ \mu\text{m}$  (Hoogzaad *et al.*, 2002; Molster *et al.*, 2002; Waters *et al.*, 1996). The abundance of crystalline silicates is typically on the order of 5 to 15% by mass (Waters, 2004) but, if the dust resides in a disc (or torus), then the crystalline fraction can be higher (Molster *et al.*, 1999).

In C-rich post-AGB stars a strong dust feature is sometimes observed at  $21\ \mu\text{m}$  (discovered by Kwok *et al.*, 1989). Also, the  $11.3\ \mu\text{m}$  feature due to amorphous silicon carbide SiC (Gilra, 1973) and the  $30\ \mu\text{m}$  band attributed to MgS (Forrest *et al.*, 1981) are important IR signatures of C-rich stars.

## 2.5 Dual Chemistry sources

Dual chemistry (or mixed chemistry) sources can be defined as sources that simultaneously exhibit O-rich and C-rich dust features in their spectra.

The IRAS LRS spectra of a number of optically bright carbon stars containing strong emission from O-rich amorphous silicates were the first to show *dual chemistry*. Nine out of the 304 sources studied by Willems & Jong (1986) have a  $9.7\ \mu\text{m}$  silicate dust emission feature in a C-rich sample.

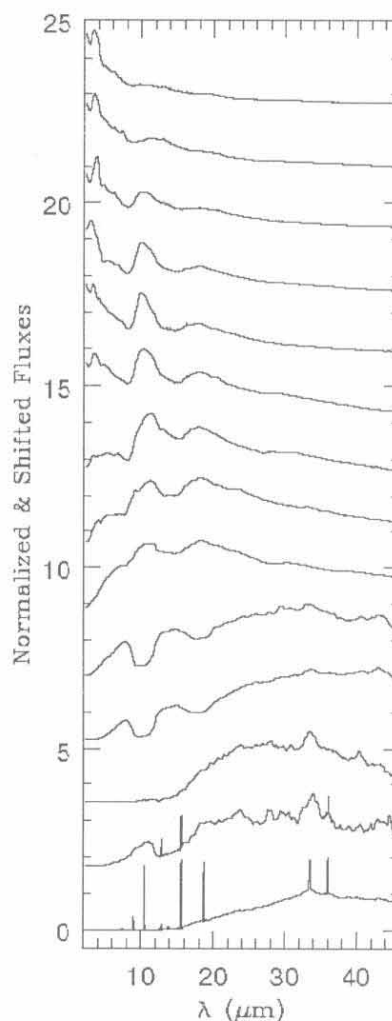


Figure 2.2: Evolutionary sequence for O-rich stars, from AGB stars to PNe (Garcia-Lario & Calderon, 2003), from top to bottom.

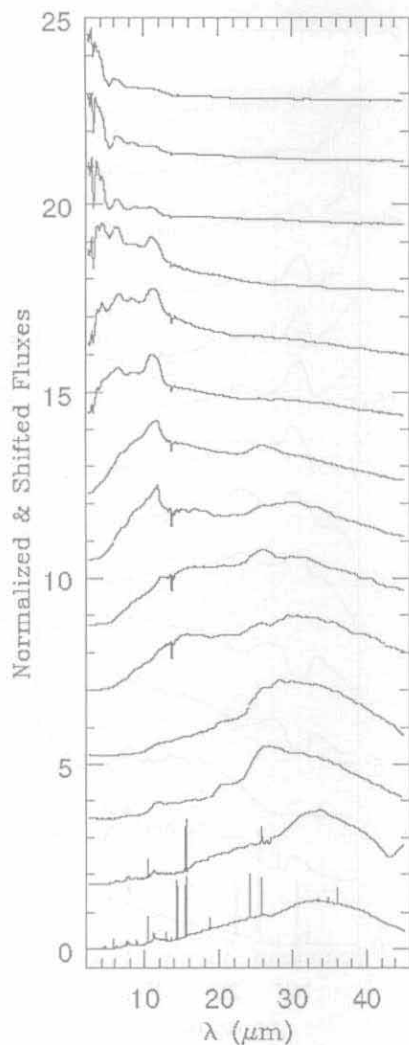


Figure 2.3: Evolutionary sequence for C-rich stars, from AGB stars to PNe (García-Lario & Calderon, 2003), from top to bottom.

Two possible scenarios were proposed to explain the dual chemistry sources: the star is being observed when a change in chemistry has *just* occurred (Willems & Jong, 1986); or a binary model (Little-Marenin, 1986) where a stable O-rich dust formation (a disc or torus) antedated a more recent C-rich transition in the central object thus creating a C-rich outflow. A possible third scenario was proposed by Waters (2004). He argues that in *all* cases, if the cool O-rich dust is located at greater distance than the innermost C-rich dust very similar dust features would be observed, and this would agree with the comet thesis (Cohen *et al.*, 1999). In this third scenario the O-rich material resides further away from the central star and the C-rich material is close to the central object. This is precisely the opposite as described in torus/disc scenario. This O-rich material would be similar to the Oort cloud present in our own solar system.

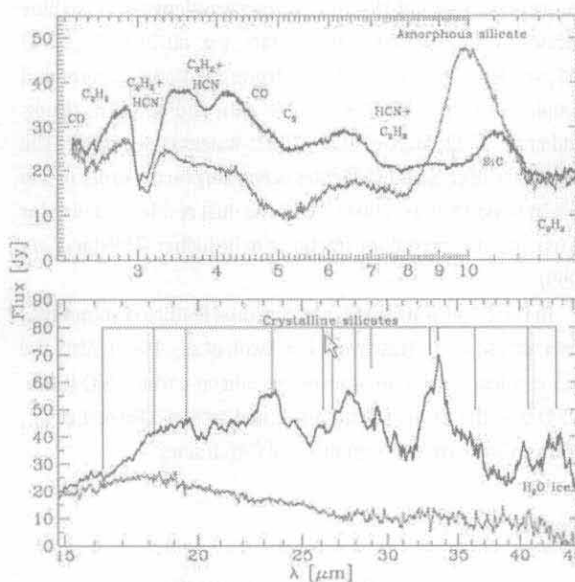


Figure 2.4: Spectrum of IRAS 09425 - 6040, solid line, and spectrum of V779 Cyg star, dotted line (Molster *et al.*, 2001).

As examples of dual chemistry objects, in figure 2.4 (Molster *et al.*, 2001), spectra of two stars with dual chemistry signatures is shown.

## 2.6 The role of binaries

It is now accepted that binaries are important in understand-



ding dual chemistry systems (Van Winckel, 2003). When Trams *et al.* (1991) observed for the first time hot dust ( $T_{\text{dust}} \sim 1,000\text{K}$ ) in post-AGB stars, it was interpreted as resulting from heavy mass loss. However, a different interpretation was needed because the mass loss needed to have this dust around the star would imply a strong decrease in the lifetime for the post-AGB phase. This would imply that a very small number of objects would be observable. Binaries are part of the solution.

Radial velocity measurements can provide direct proof of binarity (de Ruyter *et al.*, 2005). However, when the central star is too obscured, binarity can be deduced from morphological properties of the outflow. The presence of a disc appears to be common in post-AGB stars and Van Winckel (2004) argues that this implies binarity. This is also the basis for the explanation of the bipolar geometry of many post-AGB stars (e.g. Soker, 2002, 2005).

A systematic search for binary post-AGB stars is ongoing (Van Winckel, 2004) and some results are already available (figure 2.5).

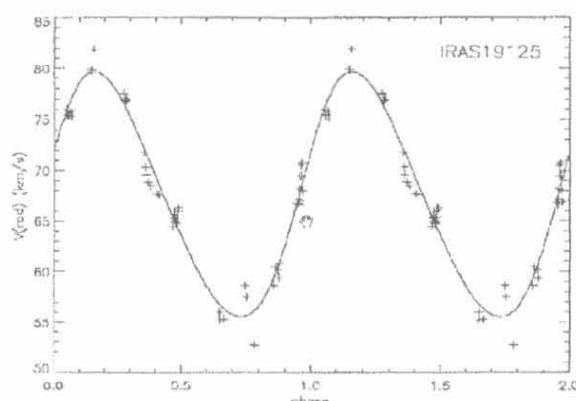


Figure 2.5: Radial velocity curve of post-AGB binary star IRAS 19125 + 0343 from Van Winckel (2004). The line is the binary orbit fit for: period of 508 days; eccentricity of 0.12 and  $A \times \sin i = 0.56\text{AU}$ .

## 2.7 PN formation

When the surface temperature of the central source becomes higher than  $\sim 3 \times 10^4\text{K}$ , the energy of the photons emitted is such that the circumstellar material is ionised. The emission lines in the spectrum emerge and this marks the

beginning of the PN phase. The chemistry of the central star depends on the nature of the star when it left the TP-AGB phase. PNe can have a surprisingly variety of morphologies (Balick, 2002, figure 1).

A review of the state of observational and theoretical studies of the shaping of PNe can be found in Balick (2002)

## 3 - Radiative Transfer

This Chapter presents a discussion of the Radiative Transfer problem (section 3.1) as well as a description of the interaction of dust and radiation (section 3.2). Then two RT computational codes are presented: DART, a ray-tracing code (section 3.3) and CSRE, a newly developed (Whitney *et al.*, 2003a) Monte Carlo radiative equilibrium code (section 3.4). The modifications made to CSRE to enable modelling of post-AGB stars are described in section 3.5 and a comparison between DART and CSRE code is presented in section 3.6.

The two RT codes presented in this Chapter are based on the physical theory of radiative transfer in dusty mediums. The fundamental equations that illustrate this theory are described here, and this description is based on and follows the notation of Carroll & Ostie (1996); Efstathiou & Rowan-Robinson (1990); Ueta (2002).

The CSRE code, described in section 3.4.1, page 24, has been created and developed by Whitney *et al.* (2003a). The code has been used to model protostellar objects (e.g., Whitney *et al.*, 2003b).

The modifications made to CSRE during our programme of research are described in detail in section 3.5, page 40, and can be divided into two categories:

- dust grain properties (section 3.5.1)
- density function and dust regions (section 3.5.2)

The aim of these modifications is to be able to make CSRE more adequate to model post-AGB stars.

### 3.1 Fundamentals of Radiative Transfer

The aim of this section is to reveal the physical equations that underpin the DART and CSRE codes, in a logical and consistent way. These equations are then used in the DART and CSRE RT codes, sections 3.3 and 3.4.

Radiative Transfer Theory is a macroscopic theory. The approximation is valid when the linear scale of the system is very much larger than the wavelength of the electromagnetic

radiation. Under this assumption, the concepts of *specific intensity*,  $I_\nu$ , and *radiative rays* i.e. radiation travels in straight lines, are used as fundamental variables of the theory.

Consider an area  $dA$  normal to the direction of a given ray. All rays passing through  $dA$  whose direction is within a solid angle  $d\Omega$  of the given ray, in the time  $dt$ , in the frequency range  $d\nu$ , have an energy  $dE_\nu$ .  $dE_\nu$  is given by,

$$dE_\nu = I_\nu dA dt d\Omega d\nu \quad (3.1)$$

Equation 3.1 is the definition of specific intensity. The dimension and units of  $I_\nu$  are:

$$\begin{aligned} [I_\nu(\nu, \nu, \Omega)] &= \text{energy} \times \text{time}^{-1} \times \text{area}^{-1} \times \text{solid angle}^{-1} \times \text{freq}^{-1} \\ &= \text{erg} \times \text{s}^{-1} \times \text{cm}^{-2} \times \text{ster}^{-1} \times \text{Hz}^{-1} \end{aligned} \quad (3.2)$$

$d\nu$  and  $dt$  are presumed to be infinitesimally small (hence their formal denomination) but, the energy uncertainty principle implies that,  $dE dt \geq h \Leftrightarrow d\nu dt \geq 1$ . This is in fact a macroscopic approximation and it is not valid on an atomic scale. However, because CSRE and DART codes implement radiative transfer on dust particles only, this is a valid theory, provided the extinction and scattering properties are correctly calculated from the electromagnetic theory (section 3.2).

The aim of building radiative transfer codes is to determine the values of  $I_\nu$  and the temperature at every point of the circumstellar envelope. These functions are found as a result of a self-consistent solution of the equation of radiative transfer,

$$\frac{dI_\nu}{d\tau_\nu} = -I_\nu + S_\nu \quad (3.3)$$

where  $S_\nu$  is called the source function. The source function describes the absorption and scattering from dust grains and  $\tau_\nu$  is the optical depth along a ray.

The source function describes the emission and absorption from dust grains and assuming that these are in thermal equilibrium,  $S_\nu$  is,

$$S_\nu = \frac{k_\nu B_\nu(T_d) + \sigma_\nu J_\nu}{k_\nu + \sigma_\nu} \quad (3.4)$$

where  $k_\nu$  is the absorption coefficient,  $\sigma_\nu$  is the scattering cross section,  $B_\nu(T_d)$  is the Planck function associated with the dust temperature,  $T_d$ , and  $J_\nu$  is the mean specific intensity ( $J_\nu = \int I_\nu d\Omega$ ).

It is possible to write a formal solution for equation 3.3 considering all quantities as functions of  $\tau_\nu$  and using the integrating factor  $e^{-\tau_\nu}$ ,

$$I_\nu = \int S_\nu e^{-\tau_\nu} d\tau_\nu \quad (3.5)$$

The real problem in solving the radiative transfer problem is that the radiation field depends upon itself as well as the temperature function. This is clear from the dependence of the source function on the temperature  $T$  and  $J_\nu$  (equation 3.4) and from the formal solution (equation 3.5). Any radiative code, either using a ray-tracing approach (section 3.3) or a monte carlo method (section 3.4), must solve this crucial problem in a self-consistent way.

### 3.2 Interaction of dust with radiation

The interaction of a dust grain with radiation determines the results obtained from the radiative transfer under consideration. This is a central and common part to both codes described in the next sections, and therefore it will be discussed prior to the explanation of the codes.

From the point of view of an observer, when radiation is propagated through a dusty medium (e.g., the ISM or a circumstellar envelope), what the observer measures is the combined effect of absorption and scattering of the radiation. This effect is the extinction caused by the dust grains interacting with radiation.

This is an interdisciplinary area of research where astrophysics meets chemistry. Astro-Chemistry is growing and its focus is on the link between the laboratory and telescopes, trying to bring together observational and theoretical astronomers, instrument



specialists and laboratory chemists. In a recent conference<sup>2</sup> (Ward-Thompson, 2005), it was suggested that future observational programmes in astronomy should include funding for parallel research in the laboratory.

As far as radiative transfer in astrophysics is concerned, the interaction of dust with electromagnetic radiation would be impossible without the laboratory-measured real and imaginary parts of the complex refractive index ( $m = n + i k$ ). These  $n$  &  $k$  values are determined in laboratory for each relevant chemical mineral, considering if the mineral is in neutral or electric charged mode.

The cross-sectional area for the interaction of a spherical grain of radius  $a$  is not given by the *natural* result of  $\pi a^2$ , but by  $Q a^2$ , where the quantity  $Q$  depends on the nature of the grain and the wavelength of the incident radiation. Mie theory (e.g. Bohren & Huffman, 1983) is used to determine the extinction, absorption and scattering cross section ( $C_{\text{ext}} = C_{\text{abs}} + C_{\text{sca}}$ ) needed to develop the radiative transfer codes. This theory is based on the following assumptions. When a plane electromagnetic wave interacts with a spherical dust particle then the scattering is:

- elastic
- incoherent (the phases of the scattered waves are not all in phase)
- single (only one scattering particle is considered for each incident wave)

For a plane electromagnetic wave incident on a dust particle of radius  $a$ , and of refractive index  $m = n + i k$ , the extinction and scattering cross sections  $C_{\text{ext}}$  and  $C_{\text{sca}}$ , are (Ueta, 2002),

$$C_{\text{sca}} = Q_{\lambda}^{\text{sca}} \pi a^2 = \mathcal{F}(\lambda, a_p, b_p) \quad (3.6)$$

$$C_{\text{ext}} = Q_{\lambda}^{\text{ext}} \pi a^2 = \mathcal{G}(\lambda, a_p, b_p) \quad (3.7)$$

where the functions  $F$  and  $G$  are dependent on  $\lambda$  and on the scattering coefficients  $a_p$  and  $b_p$  derived from Mie theory. The scattering coefficients are functions of the complex refractive index  $m$  and the particle radius  $a$ ,

$$a_p = \mathcal{H}(m, a) \quad (3.8)$$

$$b_p = \mathcal{O}(m, a) \quad (3.9)$$

The exact expressions of the functions  $F$ ,  $G$ ,  $H$  and  $O$  are derived from theory. At the end, the problem of finding the extinction and scattering cross sections,  $C_{\text{ext}}$  and  $C_{\text{sca}}$ , is mathematically equivalent to an expansion of  $H$  and  $O$  in Besse functions and spherical harmonics. These can be calculated numerically using a recursion method.

In practice, to derive the cross sections to be used as an input in the radiative transfer code, we have to consider the grain size distribution and the abundance of the chemical species. The weighted cross sections are given by (using the notation of equation 3.4),

$$\langle C_{\text{abs}} \rangle = \sum_j \alpha_j \int_a Q_j^{\text{abs}} \pi a^2 n_j(a) da \quad (3.10)$$

$$\langle C_{\text{sca}} \rangle = \sum_j \alpha_j \int_a Q_j^{\text{sca}} \pi a^2 n_j(a) da \quad (3.11)$$

where the  $Q_j^{\text{abs}}$  and  $Q_j^{\text{sca}}$  are the  $Q$  factors (dependent on the grain size and frequency) obtained from Mie theory, the subscript  $j$  refers to the chemical dust species  $j$ ,  $\alpha_j$  is the weighting factor based on the abundance of the considered dust species  $j$ , and  $n_j(a)$  is the normalised dust size distribution of the species.

$$n_j(a) \propto a^{-\gamma} : a_{\text{min}} < a < a_{\text{max}} \quad (3.12)$$

### 3.3 Description of DART code

The DART code is a radiative transfer code developed by Efstathiou & Rowan-Robinson (1990) which solves the radiation transfer equation (equation 3.3) for an axisymmetric envelope around a star. This code allows several dust species to be included (up to seven different grain materials) and can model a grain size distribution given by equation 3.12 (modifications used in Gledhill & Yates, 2003). A brief description of DART is included here to exemplify the ray-tracing approach to the RT problem in contrast to the Monte Carlo method (section 3.4 where some benefits of using a Monte Carlo method are discussed). After describing a classical ray-tracing method it is possible to demonstrate that a Monte Carlo method can return the same quantities (e.g. the moments of the intensity,  $J_\nu$  and  $H_\nu$ ) as the more traditional method described in this section.

DART is too simple in its dust treatment because, although it can include up to seven different dust species, these dust types are all averaged to the same dust input file. The user can define the relative abundance of the different dust types but then a single dust file is generated. As a result, it is not possible to have separate dust species in different regions within the circumstellar envelope, one simply has all the dust types in all the nebula, in an average sense.

#### 3.3.1 Solution of the Radiative Transfer Equation

To numerically solve the radiation transfer equation, equation 3.3 is written in the form (using the same notation as in Efstathiou & Rowan-Robinson, 1990),

$$\frac{dI_\nu}{ds} = -C_{\nu, \text{ext}} n(r, \theta) I_\nu + C_{\nu, \text{abs}} n(r, \theta) B_\nu(T_{r, \theta}) + \frac{n(r, \theta)}{4\pi} \int I_\nu C_{\nu, \text{sca}}(\theta) d\Omega \quad (3.13)$$

where  $I_\nu$  is the specific intensity of the radiation field in some specific direction,  $s$  is the distance along a ray passing through the point  $P$  in the same direction,  $n$  is the number density of dust grains at  $P$  and  $C_{\nu, \text{abs}}$  and  $C_{\nu, \text{sca}}$  and  $C_{\nu, \text{ext}}$  are the cross sections for absorption, scattering and extinction, respectively. The integration in the third term of the equation is over solid angle and  $\theta$  is the scattering angle.

To solve equation 3.13, a grid in  $r$  and  $\theta$  is used and the intensity  $I_\nu$  is calculated by ray tracing the intensity at a number of discrete frequencies  $\nu$  and directions. If radiative equilibrium is assumed, DART considers three possible ways by which energy can contribute to the value of  $I_\nu$  at a given point  $P$ ,

1. radiation directly from the star,  $I_\nu^1$
2. radiation from thermal emission from dust grains,  $I_\nu^2$
3. scattered radiation from dust grains,  $I_\nu^3$

Therefore,

$$I_\nu = \sum_{i=1}^3 I_\nu^i \quad (3.14)$$

DART solves the radiative problem (i.e., determines  $I_\nu$  and  $T$  in points of the nebula) by calculating each  $I_\nu^i$  in a separate way, as described next. This process is valid insofar as each  $I_\nu^i$  is independent of each other. The equations 3.15 are not inter-correlated. In this case equation 3.14 is valid.

The equations satisfied by each term  $I_\nu^i$  are (Efstathiou & Rowan-Robinson, 1990),

$$\begin{aligned} \frac{dI_\nu^1}{ds} &= -Q_{\text{ext}} \pi a^2 n I_\nu^1 \\ \frac{dI_\nu^2}{ds} &= -Q_{\text{ext}} \pi a^2 n I_\nu^2 + Q_{\text{abs}} \pi a^2 n B_\nu(T) \\ \frac{dI_\nu^3}{ds} &= -Q_{\text{ext}} \pi a^2 n I_\nu^3 + Q_{\text{sca}} \pi a^2 n \frac{1}{4\pi} \int I_\nu \zeta(\theta) d\Omega \end{aligned} \quad (3.15)$$

where  $\zeta$  is the scattering phase function.

Equation 3.15 results from the relation between  $C_{\nu, \text{abs}}$  and  $C_{\nu, \text{sca}}$  and  $C_{\nu, \text{ext}}$ , the cross sections for absorption, scattering and extinction, respectively, and the corresponding efficiencies,  $Q_{\nu, \text{abs}}$  and  $Q_{\nu, \text{sca}}$  and  $Q_{\nu, \text{ext}}$ ; and

from the association between the nature of each component  $I_\nu$  and the corresponding efficiency, i.e.,

- the radiation directly from the star,  $I_\nu$ , originates from the extinction of the intensity field  $I_\nu$ , first term of equation 3.13,  $-C_{\nu, \text{ext}} n(r, \theta) I_\nu$ , and,

- the radiation from thermal emission from dust grains,  $I_\nu^2$ , originates from the sum of the same term and the absorption term dependent on the temperature,  $C_{\nu, \text{abs}} n(r, \theta) B_\nu(T, \theta)$ , and,

- the scattered radiation from dust grains,  $I_\nu^3$ , has the same common component added with the scattering term dependent on the scattering phasefunction  $\zeta(\theta)$ .

The relation between  $C_{\nu, \text{abs}}$  and  $C_{\nu, \text{sca}}$  and  $C_{\nu, \text{ext}}$ , and the corresponding efficiencies,  $Q_{\nu, \text{abs}}$  and  $Q_{\nu, \text{sca}}$  and  $Q_{\nu, \text{ext}}$  is given by  $C_{\nu, \text{abs}} = \pi a^2 Q_{\nu, \text{abs}}$ ,  $C_{\nu, \text{sca}} = \pi a^2 Q_{\nu, \text{sca}} \zeta(\theta)$ , and  $C_{\nu, \text{ext}} = a^2 Q_{\nu, \text{ext}}$ , where  $Q_{\nu, \text{ext}} = Q_{\nu, \text{abs}} + Q_{\nu, \text{sca}}$ , and  $a$  is the grain radius.

Note that the cross sections are a function of  $\pi$  multiplied by the radius squared, as this can be identified with the simple geometrical cross section of a billiard ball for example, i.e. the area of the ball's cross section. The solution for equations 3.15 is (Efstathiou & Rowan-Robinson, 1990),

$$\begin{aligned} I_\nu^1 &= \begin{cases} B_\nu(T_*) e^{-\tau_\nu} & : \theta \leq \arcsin(R_*/r) \\ 0 & : \theta > \arcsin(R_*/r) \end{cases} \quad (3.16) \\ I_\nu^2 &= \int_0^S \exp\left(-\int_0^{s'} \alpha_{\text{ext}} ds'\right) \pi a^2 Q_{\nu, \text{abs}} n(r', \theta') B_\nu(T(r', \theta')) ds \\ I_\nu^3 &= \int_0^S \exp\left(-\int_0^{s'} \alpha_{\text{ext}} ds'\right) \pi a^2 Q_{\nu, \text{abs}} n(r', \theta') J_{\text{sca}} ds \end{aligned}$$

Where

$$\alpha_{\text{ext}} = \pi a^2 n Q_{\text{ext}}, \quad J_{\text{sca}} = \frac{1}{4\pi} \int I'_\nu \zeta(\theta') d\omega', \quad \tau_\nu(r, \theta) = \int \alpha(r', \theta) dr'$$

Is the optical depth to the centre of the star, and  $S$  is the distance from  $P$  to the edge of the cloud along  $s$  and  $S'$  is the distance of the point with coordinates  $(r', \theta')$  from  $P$ .

The expression for  $I_\nu$ , the radiation directly from the star, in equation 3.16 can be interpreted as follows.  $I_\nu$  will have two

solutions, one corresponding to rays inside the solid angle defined by  $P$ , the point where we are solving the equation of radiative transfer (equation 3.13), and the star (cross section of the star); and a second solution for the radiation originating outside this solid angle. The former, geometrically defined by  $\theta \leq \arcsin(R_*/r)$ ,  $R_*$  is the radius of the star, is simply the radiation produced from the central star (assumed to radiate as a blackbody,  $B_\nu(T)$ ) after being attenuated by the optical depth to the centre of the star ( $\tau_\nu = \int_{r_1}^r \pi a^2 n Q_{\nu, \text{ext}} dr$ ). The latter is zero as there is no contribution from radiation coming directly from the star outside this solid angle. Substituting the expression for  $I_\nu$  defined in equation 3.16 into the first equation in 3.15 results in a correct equation.

The radiation from thermal emission from dust grains,  $I_\nu^2$ , has a more complex form and can be interpreted as follows. The dust grains that originate this component of the radiation are distributed in an envelope around the central star and therefore in order to include the radiation from these grains, one has to integrate the radiation from these grains from the point under consideration,  $P$  to the outer edge of the nebula,  $S$ . This is the meaning of the outer integral in the equation for  $I_\nu$  (3.16). The integrand in this equation is the *net* radiation that will reach  $P$  from the dust grains in all points within the nebula, i.e. The dust in the point  $(r', \theta')$  emits thermal radiation (assuming as a black-body) but this radiation will be partially absorbed along the way and this is mathematically translated in the term,  $\pi a^2 Q_{\nu, \text{abs}} n(r', \theta') B_\nu(T(r', \theta'))$ . On top of this effect, as this radiation travels from  $(r', \theta')$  to  $P$  (hence the integral limits 0 to  $S'$ ), along each specific ray, it will suffer extinction and this is taken into account by the term,  $\exp(-\int_0^{S'} \alpha_{\text{ext}} ds')$ . Therefore, as expected, this term is formally similar to the expression regarding the effect of the optical depth,  $\exp(-\tau_\nu(r, \theta))$ . Finally, the interpretation of the solution regarding  $I_\nu^3$  (equation 3.16), the scattered light, is analogous to the previous discussion. This is the case because the differential equations satisfied by the thermal radiation and the scattered radiation are formally the same but with the scattering term as the source term, i.e. the solution for the third equation in 3.15 is equal to the second equation in 3.16 but with,

$$J_{\text{sca}} = \frac{1}{4\pi} \int I'_\nu \zeta(\theta') d\omega' \quad (3.17)$$

in place of  $B_\nu(T(r', \theta'))$ .

Note that  $I$  is present in the source term for the scattered radiation (third equation in 3.16, page 20) through equation 3.17. This is the main cause of complexity in the solution of equations 3.15, page 19, (Rowan-Robinson, 1980).

To solve this difficulty, the phase function ( $\zeta\theta'$ ) is approximated as a series of polynomials (Legendre polynomials) in  $\theta'$  of which only the first two terms are used, this is  $\zeta(\theta) = 1 + b_1 \cos \theta$ . As a result of this technique, the source term  $J_{\text{sca}}$  (equation 3.17) becomes a series of moments of  $I_\nu$ ,

$$J_{\text{sca}} = J_\nu - b_1 \cos \psi H_\nu \quad (3.18)$$

where  $J_\nu$  and  $H_\nu$  are the moments of the intensity given by,

$$J_\nu = \frac{1}{2\pi} \int_0^\pi \int_{-1}^1 I_\nu d\mu d\phi \quad (3.19)$$

$$H_\nu = \frac{1}{2\pi} \int_0^\pi \int_{-1}^1 I_\nu \mu d\mu d\phi \quad (3.20)$$

where  $\mu = \cos \theta$ , is the angle between the ray and the direction defined by the two points considered and  $b_1$  is the scattering anisotropy factor (Efstathiou & Rowan-Robinson, 1990; Rowan-Robinson, 1980, and references therein).

### 3.3.1.1 Radiative Equilibrium

From section 3.1 it is clear that the challenge for a radiative transfer code is to make sure that the solution found in equation 3.16 is self consistent. This is the condition of radiative equilibrium and this section describes how this is implemented in the DART code.

The condition of radiative equilibrium is equivalent to the condition of radiative balance in all points of the circumstellar envelope. This is expressed as,

$$\int Q_{\text{abs}} J_\nu d\nu = \int Q_{\text{abs}} B_\nu(T) d\nu \quad (3.21)$$

The mean intensity  $J_\nu$  is calculated using equation 3.19 and these are the weighted integrals of  $I_\nu$  estimated over a number of discrete directions. This procedure involves numerical errors. These errors in  $J_\nu$  will propagate to the value of the temperature that is estimated from equation 3.21. At each iterative step, the temperature solution found is tested. If this solution does not satisfy the equation of radiative balance, then the temperature is corrected by a factor of  $\Delta T$ ,

$$\Delta T = \frac{\int Q_{\text{abs}} (J_\nu - B_\nu) d\nu}{\int Q_{\text{abs}} \frac{\partial B_\nu}{\partial T} d\nu} \quad (3.22)$$

The iterative process continues until  $\Delta T$  meets a predefined convergence check. Successive iterations can lead to a satisfaction of equation 3.21 to better than 1 per cent in most of the grid points, however this is not the case for regions with high optical depth or geometrically thin discs, where large errors occur.

This is a problem that is solved in a better way in the Monte Carlo code CSRE, as the next section will describe.

### 3.4 CircumStellar Radiative Equilibrium code

CSRE has been developed by Whitney, Wood, Bjorkman and Wolf (Whitney *et al.*, 2003a) and it incorporates the Monte Carlo radiative equilibrium method developed by Bjorkman & Wood (2001).

There are some strong motivations for using CSRE. The main motivation is to realistically model dust properties in circumstellar envelopes. In contrast to a more limited approach used in DART (section 3.3) with respect to the dust properties to be used and where in the envelope to use them, CSRE can handle up to four dust files in spatially separate regions. This possibility, only available in CSRE, is important to model complex objects. These objects only recently have become interesting to be modelled since the explosion of high resolution imaging data from the HST and the large aperture ground based telescopes revealed (very) complicated densities and illuminations patterns in a wide range of astrophysical fields of research. These complex objects (e.g., the Red Rectangle, Chapter 3) have different dust types in different regions of the envelope, thus CSRE is more appropriate to model these objects.

DART (section 3.3.2) has problems handling sharp density contrasts and regions with high optical depths (e.g., circumstellar discs), but CSRE does not have these limitations due to its Monte Carlo nature. Circumstellar discs are common

in a wide range of astrophysical systems thus the possibility to model these structures is a strong reason for choosing to use CSRE.

### 3.4.1 Radiative Transfer in the Monte Carlo Method

The fundamental principle of any Monte Carlo method is that we can sample a quantity from a probability distribution using a random number. The basic idea is that if the values of physical quantities (e.g., the optical depth) can be characterised by continuous distributions in the interval  $[0, 1]$ , then these physical quantities can be simulated by a random number generator.

Compared with the classical ray-tracing solution, to solve the radiative transfer problem under a Monte Carlo<sup>3</sup> method one has to adopt a different view point. There are fewer equations to consider (not even the radiative transfer equation!) and, most important, in the heart of any Monte Carlo simulation there are probabilities.

#### 3.4.1.1 Basic Concepts

The electromagnetic radiation is divided into photon packets and these photons packets propagate through the circumstellar envelope until all of them escape. Each packet has a direction of travel and a energy,  $dE_\nu$ , and the relation between these sets of photons and the specific intensity defined in equation 3.1 is,

$$I_\nu = \frac{dE_\nu}{\cos \theta dA dt d\nu d\Omega} \quad (3.23)$$

where  $\theta$  is the angle between the radiation field to the surface normal (assumed  $\theta = 0$  in equation 3.1). Equation 3.23 is the same equation as 3.1.

The photon packet, or *photon*, represents the energy  $dE_\nu$ . The photons interact with the dust grains and this probabilistic interaction is determined by the frequency of the incident photon, scattering and absorption cross sections of the dust grain.

The properties of the dust grains used in CSRE are generated in the same way as for the DART code. This is described in section 3.2, therefore these are assumed to be an input to the code.

The photons are emitted from the central source and may escape without interacting with the circumstellar envelope. The probability that a photon interacts with a dust particle over a length  $dL$  is  $n\sigma dL$ , where  $n$  is the number density of dust grains,  $\sigma$  is the extinction cross section. If we divide the macroscopic length  $L$  into  $N$  infinitesimal lengths  $dL$ , the probability of travelling the distance  $L$  with no interactions,  $P(L)$  is the probability of no interactions in every one of the  $N$  single paths  $dL$ , i.e.  $P(dL) = (1 - n\sigma dL)$ . So,

$$P(L) = \left(1 - \frac{n\sigma L}{N}\right)^N \quad (3.24)$$

The Euler limit formula holds,

$$e^x = \lim_{n \rightarrow \infty} \left(1 + \frac{x}{n}\right)^n \quad (3.25)$$

Thus,

$$P(L) = \left(1 - \frac{n\sigma L}{N}\right)^N = e^{-n\sigma L} = e^{-\tau} \quad (3.26)$$

where  $\tau = n\sigma L$  is the optical depth. Physically, the optical depth over a distance  $L$  in a given direction is the number of photons mean free paths over  $L$ .

In general,

$$\tau = \int_0^L n\sigma ds = \int_0^L \rho k ds \quad (3.27)$$

The optical depth is (in general) wavelength dependent due to the dependence of the opacity ( $k$ ) on the absorbing and scattering species.

#### 3.4.1.2 Interaction

After the photon has travelled the interaction length one of two things can occur:

- the photon is absorbed, or
- the photon is scattered.

It is a random number that decides what happens next. The albedo  $a$  has values within  $0 < a < 1$  (defined in equation 3.28) and is the probability that the photon is scattered. This fraction is

<sup>3</sup> The Monte Carlo derived its name from the well known gambling town in France where

the ratio between the number of times the photon is scattered over number of all events (extinction). A random number  $\ell$ , in the range  $0 < \ell < 1$ , from an uniform probability distribution, is generated and if  $\ell < a$  then the photon is scattered. If  $\ell > a$  then photon is absorbed.

The albedo is defined as,

$$a = \frac{n_s \sigma_s}{n_s \sigma_s + n_a \sigma_a} \quad (3.28)$$

where the subscripts refer to the number densities and cross sections of scatterers ( $s$ ) and absorbers ( $a$ ).

If a photon is scattered it then travels in a new direction that is determined by the angular phase function of the scattering particle. The phase function is defined in section 3.4.1.4.

#### 3.4.1.3 Sampling from a Cumulative Distribution Function

In order to sample a quantity ( $\tau$  or  $\chi$ , the scattering angle) randomly from a probability distribution function (there are several ways), CSRE uses a cumulative distributive function.

To sample a quantity  $x_0$  from a probability distribution function  $P(x)$  (normalised) the cumulative probability distribution function is used,

$$\ell = \int_a^{x_0} P(x) dx \quad (3.29)$$

Where  $\ell$  is a random number sampled uniformly from the range 0 to 1,  $a$  is the lower limit of the range over which  $x$  is defined.

The probability that a photon travels an optical depth  $\tau$  without interaction is  $e^{-\tau}$ . The probability of scattering prior to  $\tau$  (cumulative) is  $1 - e^{-\tau}$ . Therefore we can sample by using,

$$\begin{aligned} \ell &= 1 - e^{-\tau} \\ \tau &= -\log(1 - \ell) \end{aligned} \quad (3.30)$$

Having sampled  $\tau$  (using the random number  $\ell$ ) in this way,  $L$  can be calculated

From,

$$\tau = \int_0^L n \sigma ds = \int_0^L \rho k ds \quad (3.31)$$

Finding  $L$  from the above equation is the process that takes the largest percentage of cpu time in this Monte Carlo method. In general this equation cannot be solved analytically and the numerical techniques can be computationally intensive.

#### 3.4.1.4 Dust Scattering

The simplest scattering phase function, isotropic scattering, can be used in CSRE, but in general, the code uses the Heney-Greenstein (HG) function as the scattering phase function.

The HG phase function,  $\Phi$ , is used to sample the scattering angle  $\theta$  for each photon packet. This function depends on the scattering asymmetric parameter  $g$  (ranging from -1 for backward-throwing scattering, 0 for isotropic scattering to 1 for forward-throwing) and the albedo  $a$  calculated at each wavelength from the grain file.

The asymmetric parameter  $g$  is defined as,

$$g = \langle \cos \omega \rangle = \frac{\int_0^\pi \Phi(\omega) \cos \omega \sin \omega d\omega}{\int_0^\pi \Phi(\omega) \sin \omega d\omega} \quad (3.32)$$

where  $\omega$  is the scattering angle measured from the angle of incident, and  $\Phi$  is the scattering phase function.

The use of HG phase function is relatively common in radiative transfer codes (e.g., Ueta, 2002, and references therein), but it is an empirical expression as it is not derive from basic principles. This can be a disadvantage of CSRE compared with DART, since the HG function is only used in CSRE.

We argue that an overall comparison between the potential of CSRE and DART, in modelling astro-physical systems, results in the clear conclusion that CSRE should be preferred in the majority of cases (section 3.6). There can, however, be identified a few disadvantages of the monte carlo method (CSRE), and these are described in the following paragraphs.

In addition to the use of the HG scattering phase function, the input file, used in DART, containing the dust properties is simpler that the one used in CSRE, e.g. it does include the scattering assymetry parameter (equation 3.32) at every wavelength. As a result, the dust properties used in CSRE are more complex and try to be physically more realistic, but this is achieved in exchange of CSRE having more free parameters than DART with respect to the dust properties used, and this can lead to smaller degree of confidence in the results of the simulation.

Another limitation of the CSRE code is that it cannot be used to systems where the opacities are temperature-dependent, as is the case in photoionized gaseous nebulae (Ercolano, 2002). This is irrelevant for the present study of post-AGB stars because dust is assumed to have temperature-independent opacity.

Finally, CSRE relies on random numbers, and this can be an



important drawback if the random number generator is not adequate for the amount of random numbers used in each simulation. A more in-depth discussion on this topic is presented in section 3.4.1.9.

### 3.4.1.5 Monte Carlo Radiative Equilibrium

This section is equivalent to section 3.3.1.1, from the DART code.

As described in section 3.4.1.2, the interaction of each photon, after being stochastically emitted by the centre source and having travelled a distance  $L$  determined by the optical depth (equation 3.31), with the extended dusty envelope can result in the photon being scattered or absorbed. This probability is defined by the dust properties at the interaction point in the nebula, and is given by the dust density and the scattering and absorption cross sections, i.e. The albedo (equation 3.28). If our random dice (see section 3.4.1.9, for a discussion on how random is our random number generator) decides that the photon is scattered then the photon travels to a new interaction point<sup>4</sup> where the process is repeated. If however the photon is absorbed, its energy (given by equation 3.33) is added to the local cell in the envelope. This produces an increment in the local temperature.

How does this process ensures the conservation of energy? When a photon is absorbed the photon's energy is added to the local cell but, to *conserve energy*, the photon is reemitted at once. These reemitted photons comprise the diffuse radiation field. The photon is reemitted at a new frequency which is determined by the corrected temperature. This process of interaction, either scattering or absorption plus reemission, described above, continues until every single photon escapes the dusty envelope, i.e. until all the new interaction points geometrically lay outside the user-defined envelope. The basic idea is that CSRE injects  $N$  photons into the envelope (which represent a total energy  $E$ ), and the code stops only when exactly  $N$  photons (representing the same energy  $E$ ) leave the envelope, therefore energy is conserved.

This process calculates both the temperature structure and the SED.

The source luminosity,  $L$ , is divided into  $N$  photon packets. So,

$$E_\gamma = \frac{L}{N} \quad (3.33)$$

$E_\gamma$  is the energy of each photon packet and each photon packet has the same energy (Bjorkman & Wood, 2001, section 2). The envelope is divided into spatial grid cells. The choice of the cell size used is discussed in the following paragraphs.

CSRE uses a three-dimensional grid in order to include arbitrary density functions (Whitney et al., 2003a). The dust density is constant within each grid cell thus in order to have a good agreement between the analytically user-defined 3D density function and the density used in the code, it is of paramount importance that the grid of cells is well chosen with respect to the defined density function. This is done by having a variable spacing cell size  $\theta$  in  $r$  and in order to sample the potentially sharp density variations and gradients in size scales from different regions in the envelope, e.g. an inner torus or disc in contrast with a more diffuse envelope or cavity.

CSRE defines a logarithmic spacing of cells in the radial direction only in the inner region of the nebula, i.e. the cell size is smaller and grows slower in the torus/disc region (close to the central star), compared to the outer regions. Further away from the star the radial spacing follows a power-law spacing, where the cells do resolve the density function even with larger cell sizes because the density function is smoother.

Then the (monochromatic) photon is injected into this grid of cells representing the envelope and it is assigned to it a frequency randomly chosen from the SED (spectral energy distribution) of the source (blackbody or a stellar atmospheric model) (Whitney et al., 2003a). This frequency determines the dust opacity per mass,  $k_\nu$ , and scattering parameters for the photon's random walk through the envelope.

$N_i$  is the number of photons absorbed in the  $i^{\text{th}}$  cell, and its energy is deposited and the cell's temperature is recalculated. The total energy absorbed in the cell is  $E_i^{\text{abs}} = N_i E_\gamma$ . Assuming local thermodynamic equilibrium and a single average dust temperature  $T$ , independent of grain size, the absorbed energy must be reradiated. The emissivity of the dust is given by  $j_\nu = k_\nu \rho B_\nu(T)$ , where  $B$  is the Planck function. The emitted energy is,

$$\begin{aligned} E_i^{\text{em}} &= 4\pi \int k_\nu \rho B_\nu(T) d\nu dV_i \\ E_i^{\text{em}} &= 4\pi \int k_P(T) \rho B(T) dV_i \end{aligned} \quad (3.35)$$

where  $dV_i$  is the cell volume,  $k_P$  is the Planck mean opacity and  $B(T) = \sigma T_i^4 \pi^{-1}$  is the integrated Planck function,  $\sigma$  is the Stefan-Boltzmann constant. If  $T_i$  is the constant temperature throughout the grid cell, then,

$$E_i^{\text{em}} = 4\pi k_P(T_i) B(T_i) m_i \quad (3.36)$$

<sup>4</sup> The new interaction point can be located outside the physical dimensions of the envelope, in which case the photon exits the system fate is decided with a throw of a random dice.

where  $m_i$  is the mass of the cell.

Equating the absorbed and emitted energy,  $E_i^{\text{abs}} = N_i E_\gamma$  and  $E_i^{\text{em}} = 4 \pi K_P (T_i) B(T_i) m_i$ , the dust temperature, after absorbing  $N_i$  photons is,

$$\begin{aligned} E_i^{\text{abs}} &= N_i E_\gamma = \frac{N_i L}{N} \\ E_i^{\text{em}} &= 4 \pi K_P (T_i) B(T_i) m_i \\ B(T) = \sigma T^4 \pi^{-1} \Rightarrow T_i^4 &= \frac{N_i L}{4 \sigma N K_P (T_i) m_i} \end{aligned} \quad (3.37)$$

$K_P$  is a real function of temperature, so this equation is solved by iteration.

Before the cell absorbs one photon, the cell has already emitted photons that carried away energy given by the cell's emissivity,  $j_\nu = k_\nu B_\nu(T_i - \Delta T)$ , where  $\Delta T$  is the change in temperature due to the absorption of this photon.

$k_\nu B_\nu(T_i)$  is the total energy that should be reradiated at the new temperature, so  $\Delta j_\nu = k_\nu [B_\nu(T_i) - B(T_i - \Delta T)]$ . If  $E_\gamma$  is small,  $\Delta T$

is small, so,

$$\Delta j_\nu \approx k_\nu \Delta T \frac{dB_\nu}{dT} \quad (3.38)$$

Thus, to correct (temperature correction) the previously emitted spectrum, the photon is reemitted with a frequency chosen from the normalised probability distribution,

$$\frac{dP_i}{d\nu} = K^{-1} k_\nu \left( \frac{dB_\nu}{dT} \right)_{T=T_i} \quad (3.39)$$

where the normalisation constant is  $K$ .

The photon's frequency has changed, so the opacity and scattering parameters accordingly and we continue with,

1. scattering
2. absorption
3. temperature correction
4. Re-emission

until all the source photons escape from the system which automatically conserves energy.

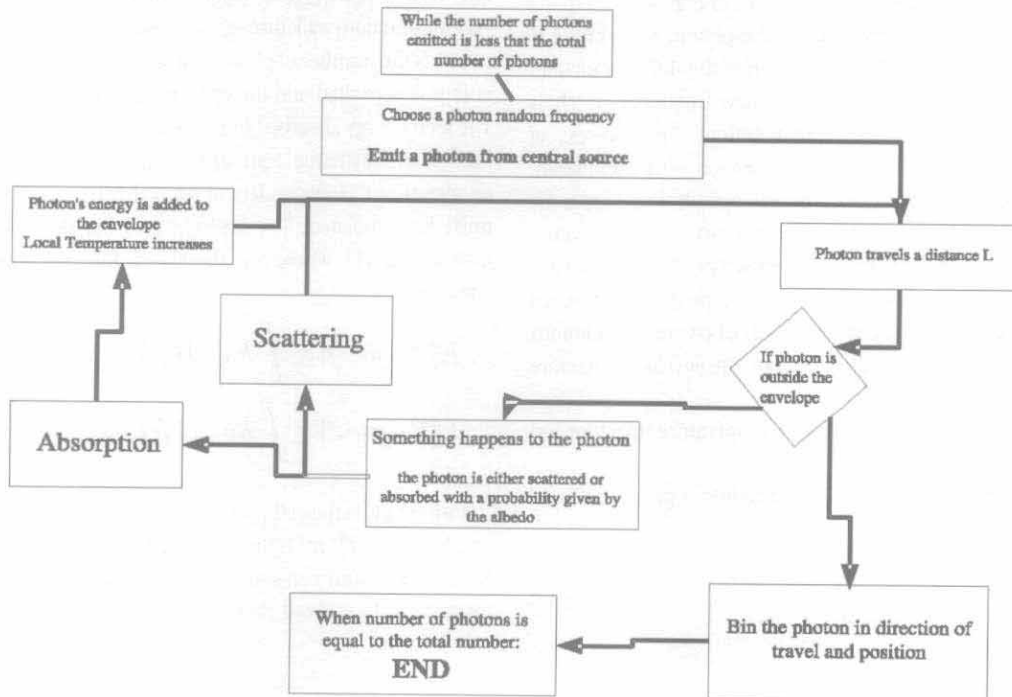


**Figure 3.1:** Photon loop flow chart. This process is repeated until all photons escape the envelope. This method implicitly conserves the total energy.

### 3.4.1.6 And the photon escapes

The code will stop when all photons exit the system (figure 3.1).

The purpose of CSRE is to measure the emergent flux (or intensity) of an astrophysical system. The flux is a continuous distribution but the Monte-Carlo method (as described in section 3.4.1) works with a discrete set of events. Therefore, CSRE is sampling the flux distribution function by binning the photons in:

- directions of travel, or angle of exit (to produce the SED),
- final position of the photon before it exited the system (to produce images).

### 3.4.1.7 Intensity Moments

The intensity moments defined in equations 3.19, are important astrophysical quantities that are an output from the solution of the equation of radiative transfer (equation 3.3) using a ray-tracing codes like DART (section 3.3.1). The values of  $J_\nu$  and  $H_\nu$  are relevant physical quantities because they measure the mean intensity and flux at each point of the circumstellar envelope, respectively.

The Monte-Carlo method can be regarded as a fast, but brut method, where is not possible to study the physical process involved in the simulation because there are no output equations, like a black-box.

Although it may be true that there are fewer equations to be considered in the CSRE compared to DART (section 3.4.1 and section 3.3, respectively), this criticism can be removed if CSRE returns the same physical quantities defined in equations 3.19, the intensity moments.

To calculate the intensity moments in the CSRE code, the contribution to the specific intensity from a single photon must be considered,  $\Delta I$ . This increment is calculated using the definition of specific intensity (equation 3.23),

$$\Delta I = \frac{\Delta E}{|\mu| \Delta A \Delta \Omega} = \frac{F}{|\mu| N \Delta \Omega} \quad (3.40)$$

where  $|\mu| = |\cos \theta|$  is the absolute value of the cosine of the angle of propagation of the photon,  $\Delta \Omega = d\mu d\phi$  is the solid angle,  $N$  is the total number of photons,  $\Delta A$  is the area,  $F = N \frac{\Delta E}{\Delta A}$  is the flux.

Substituting equation 3.40 in equations 3.19 and converting the integral to a Summation,

$$J_\nu \propto \sum_i \frac{1}{|\mu_i|} \quad (3.41)$$

$$H_\nu \propto \sum_i \frac{\mu_i}{|\mu_i|} \quad (3.42)$$

where  $\mu_i$  is the value of  $\mu$  at the centre of the bin  $i$ .

These summations are implemented in the CSRE code, thus the Monte-Carlo code can return the same quantities as the ray-tracing code.

### 3.4.1.8 Errors

The emergent flux that results from binning the photons in direction *bins* has an associated error that needs to be estimated. We are trying to measure continuous distributions using a discrete set of events, i.e. we are sampling the distribution function we wish to measure. The method to do this is to produce histograms of the distribution function, and the bins of these histograms are, by definition, the bins considered in this context.

In all Monte-Carlo simulations the error  $\delta$  approaches zero as the number of Monte-Carlo quanta  $N$  (photons packets in the CSRE case), goes to infinity. The number of photons in each bin can be described in terms of the Poisson statistics, thus the error in the flux for each direction bin is,

$$\delta \propto \frac{1}{\sqrt{N}} \quad (3.43)$$

A large number of photons must be generated for every model run with CSRE in order to reduce the error associated with the physical properties under study (equation 3.43). This is done by setting the value of the parameter  $N$  (described in table 3.1) to typical values of  $\sim 10^8$ .

### 3.4.1.9 Random Numbers

When simulating photon interactions the code is constantly calling upon random number generators (to choose optical depths and scattering angles).

The physical results from the model improve as the random number generator improves. The random number generator used in this code is the Numerical Recipes routine *ran2*. Anywhere the *ran2* is used it can be replaced by another random number generator.

Since these random numbers are generated using algorithms no output can be truly random. In fact, for the same initial conditions (input parameters, seeds) the algorithm will produce exactly the same sequence of pseudo-random numbers. The numbers are predictable. This violates the definition of random number.

In theory it is better to use true random numbers. True random numbers must be truly unpredictable. These can be generated by looking at a random process that occurs outside the computer and processing it to have random numbers available inside the computer. This true random process can be little variations in somebody's mouse movement, the amount of time between keystrokes<sup>5</sup>, the atmospheric noise from a radio (Haahr, 2005), or taking pictures of volcanic lava with a CCD (Noll & Cooper, 2005).

In practice, the implementation of true random numbers to CSRE is impossible because of the large number of random

numbers used in each run and the high precision needed. In a typical run, CSRE uses  $\sim 2 \times 10^{10}$  random numbers with a precision, given by the pseudo-random generator, of 32 bits per point. To match this, for a single CSRE model, one needs  $2 \times 10^{10} \times 32 \text{ bits} = 8 \times 10^{10} \text{ bytes}$  which requires a set of 19 DVDs! It takes  $\sim 11$  weeks to generate this amount of random data using any true-random process available now (Noll & Cooper, 2005).

### 3.4.2 CSRE: Input and Output

CSRE accepts as input:

1. central source atmospheric spectrum
2. central source parameters
3. dust properties for each region in the envelope
4. envelope geometrical parameters

Table 3.1: Summary of Input parameters for CSRE code

Parameter	Description
Preliminaries	
$N_P$	number of photons to be used (this is the number of Monte-Carlo quanta to be used)
$i$	seed used in the (pseudo-)random number generator (section 3.4.1.9)
IWRITE	output timing information every IWRITE photons
CPEEL	YES for high signal-to-noise SEDs and images
CLIMB	YES for limb darkening of central star
ATNAME	file with central source spectrum
DUSTNAME(1)	dust file containing dust properties for disc midplane (figure 3.2)
DUSTNAME(2)	dust file containing dust properties for disc surface (figure 3.2)
DUSTNAME(3)	dust file containing dust properties for envelope (figure 3.2)
DUSTNAME(4)	dust file containing dust properties for outflow (figure 3.2)
Central Source Properties	
$R_*$ ( $R_\odot$ )	stellar radius in solar radii
$T'_\odot$ (K)	blackbody temperature of central star
Disc Properties	
$M_{\text{disc}}$ ( $M_\odot$ )	disc mass in solar masses, if $M_{\text{disc}} = 0$ then no disc is used
$R_{\text{disc}}$ (AU)	maximum disc radius in AU
$R_{\text{disc}}^0$ ( $R_*$ )	minimum disc radius in radius of the star
$z_{\text{min}}$	scale height of disc at $r = r_*$ (equation 3.47)
$\alpha$	disc density exponent (equation 3.47)
$b$	disc density exponent (equation 3.47)
Envelope Properties	
$r_{\text{max}}$ (AU)	maximum envelope radius
$r_{\text{min}}$ ( $R_*$ )	minimum envelope radius
CHOLE	YES for a model with bipolar cavities
$\theta$	opening angle of cavity wall (equation 3.45)
$\beta$	cavity wall exponent (equation 3.45)
$z_0$	height of cavity wall at the origin (equation 3.45)
Density Parameters	
$\rho_{\text{amb}}$ ( $\text{g cm}^{-3}$ )	minimum value for density
$\rho_0$ ( $\text{g cm}^{-3}$ )	envelope density at $r = r_{\text{min}}$ (equation 3.44)
$\alpha$	density exponent for envelope density (equation 3.44)
$f$	factor for ellipsoidal geometry, set to 0 for spherical envelope (equation 3.44)
$\rho_{\text{cavity}}$ ( $\text{g cm}^{-3}$ )	cavity density at $r = r_{\text{min}}$ (equation 3.46)
$\gamma$	exponent for cavity density power-law (equation 3.46)
Output Data	
$H_4$ (AU)	image half-size
APERTURE(1-3) (AU)	radii of the 3 apertures
$\Theta$	angle in the latitude coordinate for high signal-to-noise SEDs and images
$\Phi$	angle along the $\phi$ coordinate for high signal-to-noise SEDs and images

and generates as output the SED (at three different apertures and 10 different inclinations) and images (at different wavelengths).

The input for CSRE is described in table 3.1.

The output CSRE spectra are contained in the fluxes points at 10 inclinations ( $i$  is the viewing angle,  $\cos i = 0.05, 0.15, \dots, 0.85, 0.95$ ), at three different apertures sizes (APERTURE (1-3), table 3.1), for all the wavelengths calculated.

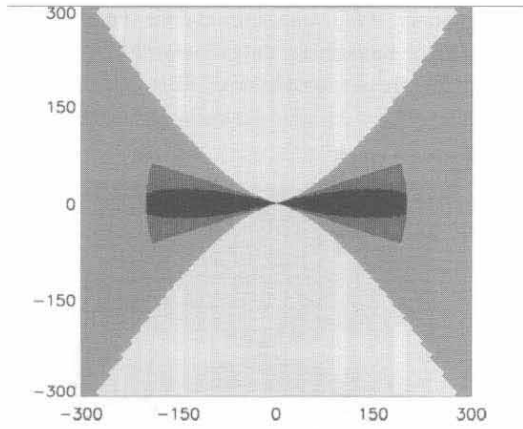


**Figure 3.2:** The four distinct regions with different dust grains properties. Black region is the disc midplane, darker grey region is the disc surface, grey is the envelope and the bipolar outflow is in lighter colour (Whitney *et al.*, 2003a, figure 1).

### 3.4.2.1 Density

The circumstellar geometry is characterised by 4 regions, the envelope, the bipolar cavity, the disc midplane and the disc surface. Each region can have different dust properties (figure 3.2). The possibility of having contrasting types of dust in different places of the circumstellar envelope is not available in DART.

The density in the envelope follows a power-law profile given by equation 3.44,

$$\rho_{\text{env}} = \frac{\rho_0 r^\alpha}{1 + (f \cos \theta)^2} \quad (3.44)$$

5 User input are in practice difficult to use because these inputs are usually buffered by the computer's operating system (several keystrokes are collected together and to the program it will seem as though the keys were pressed simultaneously).

For  $f = 0$ , this is a spherical symmetric density functions with  $\rho_{\text{env}} \propto r^\alpha$ , and for  $f > 0$ , equation 3.44 is a axial symmetric density function with factor for ellipsoidal geometry  $f$ . The input variable  $f$  was introduced to treat axisymmetric outflows from post-AGB stars.

If CHOLE is set to YES, then a bipolar cavity is carved out of the envelope. This region is adjusted by three parameters,  $\theta, \beta$  and  $z_0$ . These are the opening angle, the wall exponent and the height of cavity wall at the origin. A conical cavity with vertex at  $r = 0$  ( $\Leftrightarrow, x = y = z = 0$ ) is obtained setting  $\beta = 1$  and  $z_0 = 0$ , but a more general cavity is created for different values of these

parameters. The equation implemented in the code that shape the cavity is equation 3.45.

$$Z = z_0 + \Xi \varpi^\beta \quad (3.45)$$

where,  $Z$  is the  $z$  coordinate of a point that is located in the cavity wall,  $\varpi = \sqrt{x^2 + y^2}$  is the cylindrical radius and  $\Xi = f(\theta)$  is a function<sup>6</sup> of the opening angle,  $\theta$ .

The density in the cavity is,

$$\rho = \rho_{\text{cavity}} r^\gamma \quad (3.46)$$

Figures 3.3, 3.4, and 3.5 are 2D density plots of the equations 3.44, 3.46, and 3.47. These illustrate the density distribution in the envelope, disc and cavity, and graphically represent the geometry of the systems being modelled with this RT code.

From figures 3.3, 3.4, and 3.5, it is possible to conclude that the gradient in density is higher in the central part of the system, in particular within the disc and central part of the envelope, than within the cavities. This agrees and further justifies the choice of the cell size discussed.

The density function for the disc is given by equation 3.47. It is a flared accretion density defined by the disc parameters  $M_{\text{disc}}$ ,  $z_{\text{min}}$ ,  $a$  and  $b$  described in table 3.1 (equation 3 Whitney *et al.*, 2003a),

$$\rho_{\text{disc}} = \rho_0 \left( 1 - \sqrt{\frac{R_*}{\varpi}} \right) \left( \frac{R_*}{\varpi} \right)^a \exp \left( -\frac{1}{2} \left[ \frac{z}{\zeta(\varpi)} \right]^2 \right) \quad (3.47)$$

where  $\varpi$  is the radial coordinate at  $z = 0$ , and the scale height increases with radius as  $\zeta = \zeta_{\text{min}} \left( \frac{\varpi}{R_*} \right)^b$ .

6  $\Xi = \frac{r_{\text{max}} - z_0}{(r_{\text{max}} \tan \theta)^\beta}$ . For a conical cavity with vertices at  $r = 0$  ( $\Leftrightarrow, x = y = z = 0$ ),  $\Xi = \cot \theta$

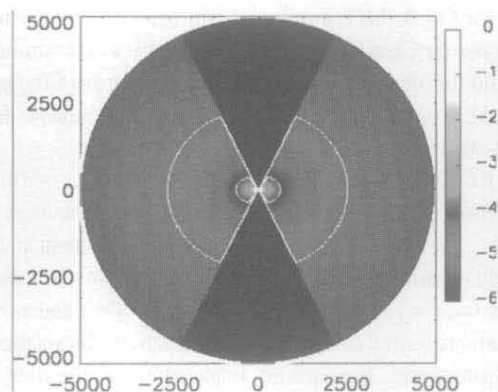


Figure 3.3: 2D plot of the density distribution in the envelope, disc, and cavity, given by equations 3.44, 3.46, and 3.47, respectively. The density colour scaling is logarithmic, plotted to 6 orders of magnitude from the peak density of  $3 \times 10^{-14} \text{ g cm}^{-3}$ , i.e. the white colour, labelled in the vertical colour bar, represents the peak density and the contours each decrease by 1 order of magnitude and match the labels in the colour bar. The  $x$  and  $y$  axis are plotted in AU (adapted from Whitney *et al.*, 2003a).

### 3.5 Modifications to CSRE

The CSRE code described in section 3.4.1 has been developed by Whitney *et al.* (2003a) to model proto-stellar objects (e.g. Whitney *et al.*, 2003b).

The modifications made to CSRE during our programme of research can be divided into two categories:

1. dust grain properties (section 3.5.1)
2. density function and dust regions (section 3.5.2)

The aim of these modifications is to be able to make CSRE more adequate to model post-AGB stars.

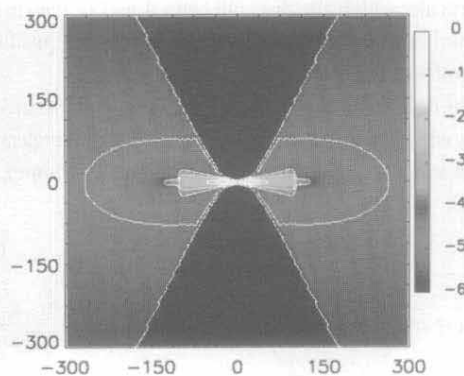


Figure 3.4: 2D plot of the density distribution in the envelope, disc, and cavity (central 300AU), given by equations 3.44, 3.46, and 3.47, respectively. The density colour scaling is logarithmic, plotted to 6 orders of magnitude from the peak density of  $1.5 \times 10^{-12} \text{ g cm}^{-3}$ , i.e. the white colour, labelled in the vertical colour bar, represents the peak density and the contours each decrease by 1 order of magnitude and match the labels in the colour bar. The  $x$  and  $y$  axis are plotted in AU (adapted from Whitney *et al.*, 2003a).

Some input parameters for the original version of CSRE (table 3.1) are no longer in use and new parameters were introduced. These are described in table 3.2.

#### 3.5.1 Dust

For the dust, it is now possible to generate dust files that can be used as input to CSRE. These files can have dust with chemical compositions, such as silicates (Ossenkopf *et al.*, 1992), silicates and graphite (Draine & Lee, 1984), amorphous carbon (Hanner, 1988), and silicon carbide (Pegourie, 1988), with any relative abundances, and grain size distribution.

These files are generated before CSRE is set to run and table 3.3 is a description of the input parameters available to generate these files.

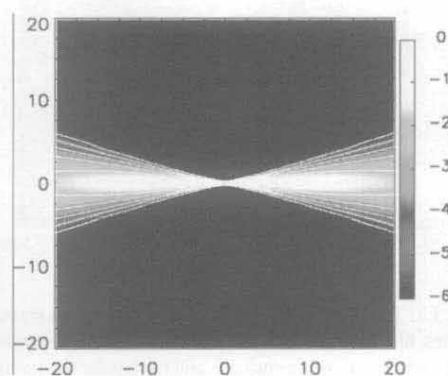


Figure 3.5: 2D plot of the density distribution in the disc, and cavity (central 20AU), given by equations 3.44, 3.46, and 3.47, respectively. The density colour scaling is logarithmic, plotted to 6 orders of magnitude from the peak density of  $8 \times 10^{-12} \text{ g cm}^{-3}$ , i.e. the white colour, labelled in the vertical colour bar, represents the peak density and the contours each decrease by 1 order of magnitude and match the labels in the colour bar. The  $x$  and  $y$  axis are plotted in AU (adapted from Whitney *et al.*, 2003a).

The modified version of CSRE expects 3 dust files (not 4 as the original version). One file for each region of the circum-stellar nebula (figure 3.7). A dust file is a table with 5 columns and each line corresponding to a value of wavelength. Every column  $i$ ,  $i = 0, 4$  (table 3.3) is a physical quantity obtained using Mie Theory (section 3.2):  $i = 0 \rightarrow$  wavelength,  $i = 1 \rightarrow$  extinction cross section,  $i = 2 \rightarrow$  scattering cross section,  $i = 3 \rightarrow$  opacity,  $i = 4 \rightarrow$  scattering asymmetry parameter.

There is a new set of parameters now in CSRE which are in the dust parameter block in table 3.2. None of these parameters is present in the original version of CSRE. These parameters, AFLAG, GFLAG and KFLAG, are used to override some input from the dust files and can be useful if one wants to run a model in which the dust scattering needs to be isotropic (for isotropic scattering, GFLAG = 0 to force  $g = 0$ ), or the albedo needs to be set to 0.5 (AFLAG = 0 to have  $a = 0.5$ ; set AFLAG = 1 to have



$a = \frac{C_{\text{dca}}}{C_{\text{ext}}}$  as read from the dust file).

The dust-to-gas ratio used in our models (models 2 and 3<sup>7</sup>), presented in section 4.3.1, is,

- $\frac{\rho_d}{\rho} = 0.01$ , for the innermost region of the circumstellar dust shell (disc or torus),
- $\frac{\rho_d}{\rho} = 0.004$ , for the envelope and cavity.

The parameter that allows the user to control the dust-to-gas ratio  $\frac{\rho_d}{\rho}$  to be used throughout the circumstellar nebula is KFLAG<sup>8</sup>. The default value, KFLAG = 1 corresponds to  $\frac{\rho_d}{\rho} = 0.01$ , however, in some post-AGB stars it may be more realistic to use different dust-to-gas ratios in different parts of the nebula (e.g. Men'shchikov *et al.*, 2002).

In this case, the user has the option to set  $\frac{\rho_d}{\rho} = 0.01$  in the innermost region of the circumstellar dust shell (region 1, defined in figures 3.6 and 3.7), and  $\frac{\rho_d}{\rho} = 0.004$  in the rest of the envelope and outflow (regions 2 and 3, figures 3.6 and 3.7).

### 3.5.2 Density and Dust regions

The density function available in the original version of CSRE is described in section 3.4.2.1, and is  $\alpha r^a$  (for some user-defined value of  $a$ ) for the envelope and outflow and a flared accretion density in the disc (equation 3.47).

In the original CSRE code, the dust regions (regions with the same dust properties) are illustrated in figure 3.2 and did not allow, for example, to have two spherical dust shells, around the central star, with different dust properties (and different densities functions) in each shell.

The user in the new version of CSRE can specify 3 dust regions and 4 density functions (region 2 may have a different density function for  $r > r_2$ ).

Region 1 is a spherical shell defined by its minimum and maximum radius,  $r_{\text{min}}$  and  $r_1$ , respectively (table 3.2). The

Table 3.2: Summary of Input parameters for the modified version of CSRE

Parameter	Description
<b>Preliminaries</b>	
$N_P$	number of photons to be used (this is the number of Monte-Carlo quanta to be used)
$i$	seed used in the (pseudo-)random number generator (section 3.4.1.9)
IWRITE	output timing information every IWRITE photons
CPEEL	YES for high signal-to-noise SEDs and images
CLIMB	YES for limb darkening of central star
ATNAME	file with central source spectrum
DUSTNAME(1)	dust file containing dust properties for disc midplane (figure 3.7)
DUSTNAME(2)	dust file containing dust properties for disc surface (figure 3.7)
DUSTNAME(3)	dust file containing dust properties for outflow (figure 3.7)
<b>Central Source Properties</b>	
$R_*$ ( $R_\odot$ )	stellar radius in solar radii
$T_\odot$ (K)	blackbody temperature of central star
<b>Envelope Properties</b>	
$r_{\text{max}}$ (AU)	maximum envelope radius
$r_{\text{min}}$ ( $R_\odot$ )	minimum envelope radius
$r_1$ ( $r_{\text{max}}$ )	maximum radius for region 1
$r_2$ ( $r_{\text{max}}$ )	characteristic radius for region 2
$r_3$ ( $r_{\text{max}}$ )	characteristic radius for region 3
CHOLF	YES for a model with bipolar cavities
$\theta$	opening angle of cavity wall
$\alpha$	cavity wall exponent
$z_0$	height of cavity wall at the origin
<b>Density Parameters</b>	
$\rho_{\text{amb}}$ ( $\text{g cm}^{-3}$ )	minimum value for density
$\rho_1^I$ ( $\text{g cm}^{-3}$ )	density at $r = \mu$
$\rho_1^{II}$ ( $\text{g cm}^{-3}$ )	density at $r = r_1$ (region 1)
$\rho_2^I$ ( $\text{g cm}^{-3}$ )	density at $r = r_1$ (region 2)
$\rho_2^{II}$ ( $\text{g cm}^{-3}$ )	density at $r = r_2$ (region 2)
$\rho_3$ ( $\text{g cm}^{-3}$ )	density at $r = r_3$
$\mu$ ( $R_\odot$ )	mean value for the Gaussian density function
$\sigma$ ( $R_\odot$ )	standard deviation for the Gaussian density function
$\beta I$	exponent I for density power-law in region 2
$\beta II$	exponent II for density power-law in region 2
$\gamma$	exponent for density power-law in region 3
<b>Dust Parameters</b>	
AFLAG	set AFLAG = 0 to force the albedo to $a = 0.5$ ; set AFLAG = 1 to have $a = \frac{C_{\text{dca}}}{C_{\text{ext}}}$
GFLAG	set GFLAG = 0 to force $g = 0$ ; else $g$ is read from dust file
KFLAG	set KFLAG = 0 to have $k = 0.4 \times k_{\text{dustfile}}$ ; else $k = k_{\text{dustfile}}$
<b>Output Data</b>	
$R_i$ (AU)	image half-size
APERITURE(1-3) (AU)	radii of the 3 apertures
$\Theta$	angle in the <i>latitude</i> coordinate for high signal-to-noise SEDs and images
$\Phi$	angle along the $\phi$ coordinate for high signal-to-noise SEDs and images

7 model 1 has a constant dust-to-gas ratio,  $\frac{\rho_d}{\rho} = 0.01$

8 KFLAG was not present in the original version of CSRE

**Table 3.3:** Summary of Input parameters used to generate the dust files

Parameter	Description
<b>Input</b>	
<b>Chemical Composition</b>	
$z_i$	fractional abundances of grains with built-in optical properties
$n(\lambda), k(\lambda)$	complex refractive index ( $n = n + ik$ ) for non built-in grains
$\sigma_{ext}, \sigma_{scat}$	extinction and scattering cross sections for non built-in grains
<b>Grain Size Distribution</b>	
$q$	exponential factor for the grain size distribution function
$a_{min} (\mu m)$	minimum grain size
$a_{max} (\mu m)$	maximum grain size
<b>Output</b>	
$\lambda$	wavelength ( $i = 0$ )
$\sigma_{ext}(\lambda)$	extinction cross section ( $i = 1$ )
$\sigma_{scat}(\lambda)$	scattering cross section ( $i = 2$ )
$k(\lambda)$	opacity or mass absorption coefficient ( $i = 3$ )
$g(\lambda)$	scattering asymmetry parameter ( $i = 4$ )

density function here has a Gaussian profile fixed by its value at  $r = \mu$  and at  $r = r_1$ , and by the Gaussian mean value and standard deviation. These are predetermined by the user in the input values of  $\rho_1^I$  and  $\rho_1^{II}$ ,  $\mu$  and  $\sigma$ , in the same order.

Region 2 is a spherical shell defined by its minimum, maximum radius and by its characteristic radius,  $r_1, r_{max}$  and  $r_2$ , respectively. The density function here follows a power law over  $r$  defined by its value at  $r_1$  and by a power-law exponent, for  $r < r_2$ , and by its value at  $r_2$  and by a power-law exponent, for  $r_2 < r < r_{max}$ .

These are predetermined by the user in the input values of  $\rho_2^I$  and  $\beta I$ ,  $\rho_2^{II}$  and  $\beta II$ , respectively.

The density function in the polar cavity is a constant function for  $r < r_3$  and has a power-law profile for  $r > r_3$ . The constant part of the density function is set by the input parameter  $\rho_3$ , and in the power-law part the density is  $\propto \rho_3^{-\gamma}$ .

The above description of the density functions and dust regions can be encapsulate in the equation 3.48 and are illustrated in figures 3.6 and 3.7.

(3.48)

$$\rho(r) = \begin{cases} \rho_1^{II} + (\rho_1^I - \rho_1^{II}) \exp\left(-\frac{(r-\mu)^2}{2\sigma^2}\right) & : r_{min} < r < r_1 \\ A \rho_2^I r^{-\beta I} & : r_1 < r < r_2 \\ B \rho_2^{II} r^{-\beta II} & : r_2 < r < r_{max} \\ \rho_3 & : z < z < r_3 \\ C \rho_3 r^{-\gamma} & : z < z \text{ and } r_3 < z \end{cases}$$

The parameters  $A, B$  and  $C$  are normalisation constants with values of  $A = r_1^{\beta I}, B = r_2^{\beta II}, C = r_3^{-\gamma}$

All other parameters present in equation 3.48 are described in table 3.2.

The disc is the region 1 in equation 3.48, i.e. the Gaussian form of the density function in region 1 can be defined by the user to represent either a disc or a torus. It is worth noticing that in this modified version of CSRE the disc as it was defined in equation 3.47, is no longer available to the user.

These density modifications were introduced to explore the flexibility of the CSRE code and specifically to simulate the density structure used by Men'shchikov *et al.* (2002) to model the Red Rectangle. Nevertheless, the CSRE code can have arbitrary density functions.

### 3.6 CSRE and DART: comparison

In order to test the validity of the CSRE and DART codes, spherically symmetric models were constructed and compared, i.e. we are comparing a monte-carlo technique with results from the ray-tracing code DART (Efstathiou & Rowan- Robinson, 1990), described in section 3.3.

The models represent a spherically symmetric dust shell having different physical characteristics, different optical depths  $AV$ , with density function only dependent on the radial coordinate  $r$  as  $\rho \propto r^{-2}$ . The shell is composed of 100% amorphous carbon (Hanner, 1988) and the other physical parameters are listed in table 3.4.

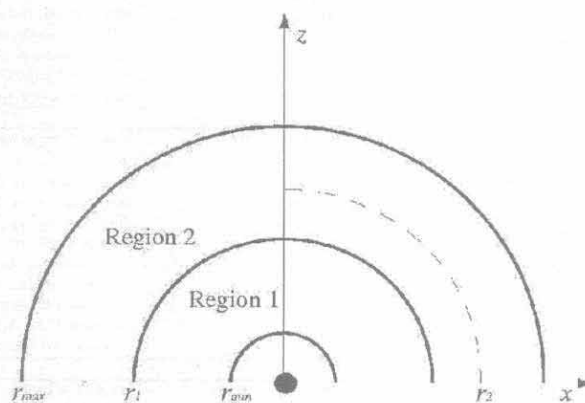


**Figure 3.6:** Schematic representation of spherical layered shell CSRE model. Solid lines divide the different dust regions. The dashed line represents the characteristic radius  $r_2$  of Region 2.

The central stellar flux model used was a model stellar atmosphere with effective temperature of 7,500K, solar metallicity and gravity  $\log g = 3.5$ .

With these parameters constant, the optical depth of the dust shell was varied,  $A_V = 1.0, 4.0, 8.0$  and  $10.0$ , with a total of 8 CSRE models. We have 4 CSRE models with the label *g* NORMAL and 4 four CSRE models labelled *g* ZERO, i.e.,

**g NORMAL** the scattering asymmetric parameter *g*, calculated using Mie theory and used to approximate the scattering phase function with the HenyGreenstein function, section 3.4.1.4

**g ZERO** isotropic scattering ( $g = 0$ )

Using the same set of parameters, *with built-in isotropic scattering*, 4 equivalent DART models were obtained for comparison.

Comparing the CSRE and DART models, figures 3.8, 3.9, 3.10 and 3.11<sup>9</sup> a good fit is observed between the dashed blue line and the crosses, which represent the DART model and the isotropic (*g* ZERO) CSRE model.

The dash-point-dash black line represents only the scattered CSRE flux for the anisotropic scattering CSRE model and it completely dominates the CSRE total SED (pink line) for  $A_V \geq 4$ , causing the isotropic and anisotropic scattering models to diverge.

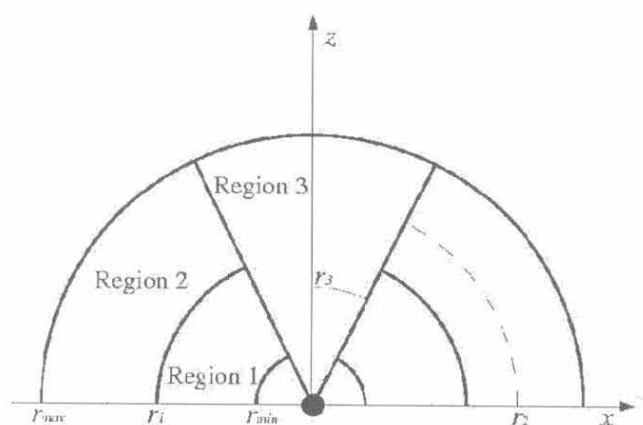


**Figure 3.7:** Schematic representation of layered shell CSRE model with bipolar cavity (compare with figure 3.2). Solid lines divide the different dust regions. The dashed line represents the characteristic radius  $r_2$  of Region 2. The fine-dashed line represents the characteristic radius  $r_3$  of Region 3.

The discussion on the SEDs presented in figures 3.8, 3.9, 3.10 and 3.11, is valid when the density distribution is spherical symmetric. In the case of a axisymmetric geometry and considering anisotropic scattering (*g* Normal), one has to take into account the viewing angle, between the observer and the system, because the SED that will be detected (through a telescope, or in a simulation) will be different for different inclinations (e.g., Whitney *et al.*, 2003a, figure 3). Moreover, the dust properties used in each individual model, i.e. the albedo, will determined the shape of the SED under the this conditions of anisotropic scattering and axisymmetry (Bjorkman & Wood, 2001; Whitney *et al.*, 2003b), thus it is difficult to generalise a relation between the anisotropic dust scattering and density axisymmetry distribution.

**Table 3.4:** Spherical Shell Model Parameters

Parameter	Value
Central Star	
$T_{\text{eff}}$ (K)	7,500
$R_*$ (cm)	$2.436 \times 10^{12}$
$d$ (pc)	710
Shell	
$r_{\text{min}}$ (cm)	$1.349 \times 10^{16}$
$r_{\text{max}}$ (cm)	$1.668 \times 10^{17}$
Dust Grains	
$a_{\text{min}}$ ( $\mu\text{m}$ )	0.01
$a_{\text{max}}$ ( $\mu\text{m}$ )	2.0
$q$	3
$A_V$	1.0 (fig. 3.8), 4.0 (fig. 3.9), 8.0 (fig. 3.10), 10.0 (fig. 3.11)

The possibility of modelling a system considering anisotropic scattering is not available in DART, thus CSRE is a much better code to use in modelling systems with a dust disc or torus.

The study of the effect of the scattering component on the total SED was only possible because CSRE is enable to separate the different SED components,

- total,
- stellar direct,
- scattered,
- thermal.

The monte-carlo method is based on discrete events, photon scattering, absorption and reemission, and it is possible to know if a photon simply escapes from the circumstellar medium without any interaction (and contribute to the stellar direct SED), or if at least one interaction has occurred (contribution to the scattered SED). We then label each specific photon as a stellar direct photon or as a scattered photon. The thermal SED is calculated by subtracting the scattering and

<sup>9</sup> The SEDs have the two-peak shape characteristic of post-AGB stars.

direct fluxes from the total flux. This is not possible in the DART code, and was crucial in the conclusion that follows.

The next paragraphs are a discussion based on figures 3.8, 3.9, 3.10 and 3.11.

From the analysis of these SEDs, one can conclude that DART should not be used to model objects with  $A_V \geq 4$  because its results diverge from the physically more realistic CSRE results. This is due to the fact that the anisotropic scattering determined in CSRE uses the values of  $g$  calculated at each wavelength for each grain size distribution and dust chemical composition whilst DART assumes isotropic scattering,  $g = \text{constant} = 0$ .

The reason why this effect occurs is as follows. For low values of optical extinction the SED is dominated by the stellar direct fluxes and the average photon is scattered a small number of times, therefore, the scattered SED is not important (because it has much lower values than the stellar direct SED). Under these conditions, DART and CSRE (with  $g = 0$ ) give the same result, however, for high values of  $A_V$ , the scattered SED is the most important contribution to the total CSRE (for  $g > 0$ ) SED, in the UV and optical wavelengths. Under these conditions, a forward-scattering phase (anisotropic scattering) function will generate a higher value of scattering fluxes because, in an envelope where the density is decreasing radially, the scattered photons have a higher probability of being scattered forward towards the direction of the viewer. More photons are propagated radially with anisotropic scattering than with isotropic scattering.

Thus, the CSRE results with  $g > 0$  produce higher values for the scattered SED compared with DART (isotropic scattering), and this component dominates the total CSRE SED at UV and optical wavelengths.

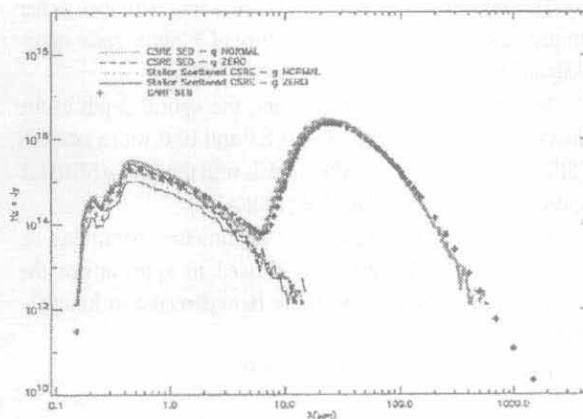


Figure 3.9: SEDs for spherical shell models with optical depth,  $A_V = 4.0$ .

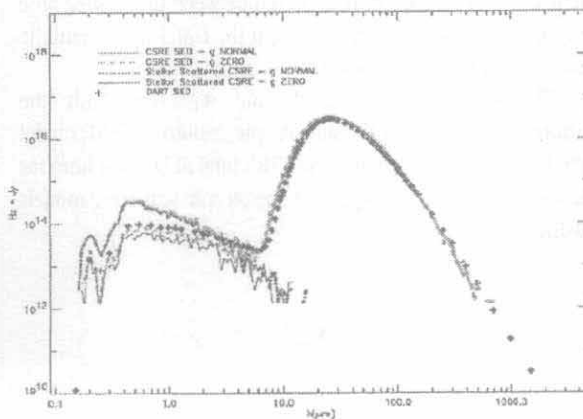


Figure 3.10: SEDs for spherical shell models with optical depth,  $A_V = 8.0$ .

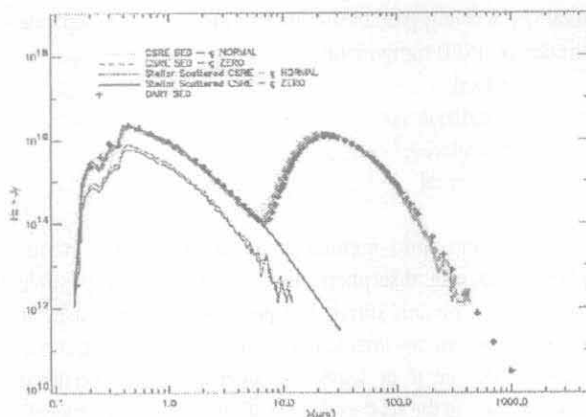


Figure 3.8: SEDs for spherical shell models with optical depth,  $A_V = 1.0$ . The black solid line (medium-thickness) is the un-obscured stellar spectrum.

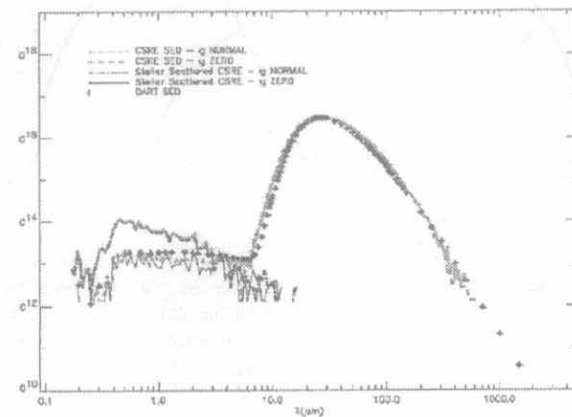


Figure 3.11: SEDs for spherical shell models with optical depth,  $A_V = 10.0$ .

## 4 - Model for the Red Rectangle

In this chapter, some observational results for the Red Rectangle (also known as HD 44179, AFGL 915, IRAS 06176-1036) are presented and the CSRE code is used to construct detailed radiative transfer models in order to derive some conclusions about the structure and physical properties of the Red Rectangle, comparing our modelling results with the published model of the same object (Men'shchikov *et al.*, 2002).

### 4.1 Introduction

The Red Rectangle is a fascinating and widely studied object. Since it was first discovered by Price & Walker (1976) and confirmed and identified as a binary star embedded in a peculiar nebula by Cohen *et al.* (1975), this object has been extensively studied during these three decades (see references in Cohen *et al.*, 2004; Men'shchikov *et al.*, 1998; Waters *et al.*, 1998). Due to its yet un-revealed secrets, the interest of the Astrophysical community is as high today as it has ever been, and a Conference dedicated exclusively to the Red Rectangle will take place in May 2006<sup>10</sup> (Allamandola *et al.*, 2006).

Some of the most interesting images available and the fluxes used to constrain our models are described in section 4.2. Section 4.3 presents our modelling and the results of it are discussed in section 4.4.

### 4.2 Observational data

The SED is generated as an output of the CSRE code therefore we are interested in all published fluxes (at any wavelength) of the Red Rectangle.

The study of the Red Rectangle presented in this chapter relies on the comparison of the SED produced by 3 different CSRE models and observed values of fluxes, i.e. the observed SED. We also present the best observational images available in the literature for the Red Rectangle (section 4.2.3) chiefly to justify the use of an axisymmetric density functions in our models (the images are clearly non-spherical), and thus the need to include a torus in the simulations.

The method followed by us, consisted in trying to obtain a fit for the SED and then investigate how good was the agreement of the synthetic images and the observed images in detail. The SED fit was not achieved with the degree of confidence needed to justify the detailed analysis of the images, therefore a preliminary analysis of the CSRE model images produced and the observed images for the Red Rectangle was inconclusive because, although the spatial extent of both sets of images was

roughly consistent, an in-depth study of the detailed structure and intensity values was not finished, thus, we argue that when the fit of the SED could be improved then further investigation into this topic is important.

#### 4.2.1 Fluxes

The observations available cover a wide range in wavelengths, from HST FOS ultraviolet  $\lambda > 0.1575 \mu\text{m}$  (Reese & Sitko, 1996) to VLA radio fluxes  $\lambda \approx 36,000 \mu\text{m}$  (Jura *et al.*, 1997). This corresponds to a range in energy between  $\sim 6 \text{ eV}$  and  $\sim 10^{-5} \text{ eV}$ . A model for the Red Rectangle is therefore well constrained within several orders of magnitude.

The observational data included in figures 4.7, 4.8 and 4.9 was published in, Allen *et al.* (1977); Cohen *et al.* (1975); Greaves & Holland (1997); Jura *et al.* (1997); Reese & Sitko (1996); van der Veen *et al.* (1994); Waters *et al.* (1998), from UV to sub-millimetre fluxes, respectively. This data was used to compare the model SEDs to the real data for the Red Rectangle.

The optical spectrum included in this work (from Reese & Sitko, 1996) only samples the central few arc-seconds around the central star and shows no extended red emission (ERE). This is consistent with the fact that our model does not contain any dust grains with chemical composition that produce this ERE. Our dust has a complex grain size distribution throughout the nebula but its chemical composition is 100% amorphous carbon (Hanner, 1988).

#### 4.2.2 Dual chemistry in the RR

The dual chemistry (defined in section 2.5) nature of the Red Rectangle is demonstrated by two strong observational sets of observations, the oxygen-rich material is responsible for the OH features at UV wavelengths (figure 4.2) and the detection of crystalline silicate emission (figure 4.1) (and CO<sub>2</sub>), whilst the carbon-rich material is responsible for the PAH emission observed in the 11.3  $\mu\text{m}$  image (figure 4.1).

Reese & Sitko (1996) published the UV spectrum of the Red Rectangle from observations taken in 1992 with the Hubble Space Telescope's Faint Object Spectrograph (figure 4.2). The range in wavelength covered is 0.1575 to 0.3286  $\mu\text{m}$  and it is dominated by CO emission between 0.16 and 0.18  $\mu\text{m}$  and at 0.2163  $\mu\text{m}$ . The features present at 0.309 and 0.3148  $\mu\text{m}$  are identified as OH emission features. These features are evidence of the dual chemistry nature of this object.

#### 4.2.3 Images

In the optical range of the electromagnetic spectrum, the best images of the Red Rectangle are present in Cohen *et al.*

<sup>10</sup> www.theredrectangle.net

(2004). In this paper, ground based images from ESO 3.5m NTT at La Silla and Hubble Space Telescope images from WFPC2 are used to create three-colour images (figures 4.3 and 4.4). In the infrared, the best images are present in Waters *et al.* (1998). These are figures 4.1 and 4.5.

### 4.3 Models

To model the Red Rectangle, we have performed model calculations using the

CSRE Monte-Carlo radiative transfer code described in section 3.4.

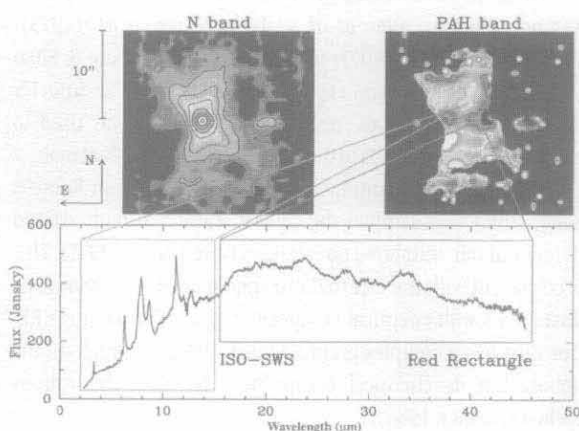


**Figure 4.1:** Top: False-colour images of the broad-band 10  $\mu\text{m}$  emission (left) and continuum subtracted narrow-band 11.3  $\mu\text{m}$  emission (right) (Waters *et al.*, 1998, figure 3). The boxes define the spatial distribution of the oxygen and carbon rich components. The broad-band 10  $\mu\text{m}$  image shows that most of the emission at that wavelength originates from circumbinary torus, and the brightness distribution of the narrow-band image at 11.3  $\mu\text{m}$  shows that the carbon-rich carriers are located in the extended nebula.

The original version of CSRE (section 3.4) and the modified version of CSRE (section 3.5) were used, and the result SEDs are presented in figures 4.7 and 4.8, respectively.

#### 4.3.1 One object, two models

This section presents two alternative models to the Red Rectangle (table 4.1), one less sophisticated model (model 1), with a envelope density power-law  $\rho \propto r^{-2}$  and with the standard interstellar size distribution  $\frac{dn}{da} = a^{-3.5}$ , and a second model (model 2) which uses the modifications to CSRE described in section 3.5 to have the central star embedded in a dusty torus in an axially-symmetric geometry defined by the biconical outflow, a variable dust-to-gas ratio and very large dust grains of constant size in the torus.

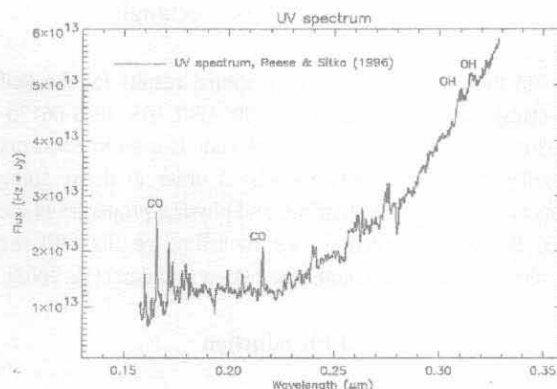


**Figure 4.2:** UV spectrum of the Red Rectangle (Reese & Sitko, 1996).

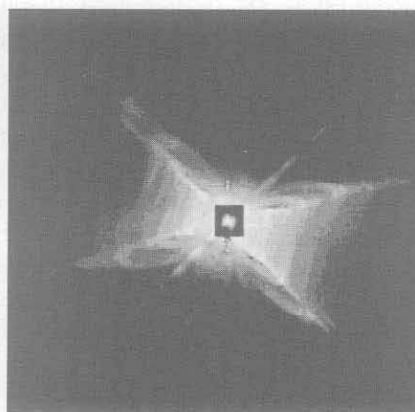


**Figure 4.3:** Three-colour rgb image in F631N - 6306 Å (red), F588M - 5893 Å (green), F467M - 4663 Å (blue). Total dimensions are  $23''.3 \times 23''.3$  (Cohen *et al.*, 2004, figure 6). North is to the bottom right (120 degrees clockwise from vertical), and east is to the top right (30 degrees clockwise from vertical).

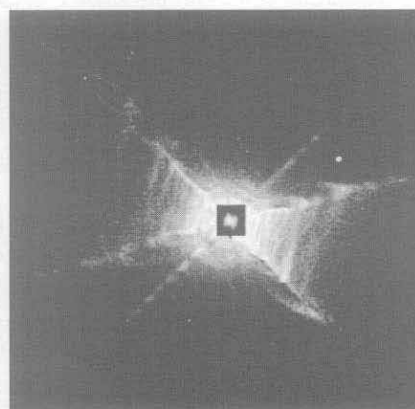


**Figure 4.4:** Three-colour rgb image in F631N - 6306 Å (red), F622W - 6131 Å (green), F588M - 5893 Å (blue). Total dimensions are  $23''.3 \times 23''.3$  (Cohen *et al.*, 2004, figure 11). North is to the bottom right (120 degrees clockwise from vertical), and east is to the top right (30 degrees clockwise from vertical).



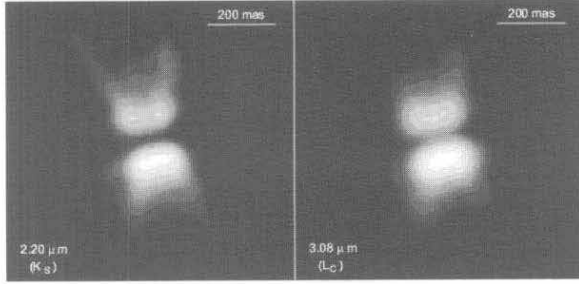


Figure 4.5: KS (2.2  $\mu\text{m}$ ), and LC (3.08  $\mu\text{m}$ ) speckle images of the Red Rectangle (Tuthill *et al.*, 2002). North is up and east is to the left.

In both models we have used a stellar atmosphere parameterised by  $T_* = 7,750\text{K}$ , gravity  $\log g = 1.5$ , metallicity  $[M/H] = -3$ , and micro-turbulent velocity of  $2\text{km s}^{-1}$ . This is the same kurucz profile used in Men'shchikov *et al.* (2002).

In Model 1, a 100% amorphous carbon (Hanner, 1988) envelope is defined between 14AU and 43,000AU, with a biconical cavity carved out (opening angle of 50 degrees) and density power-law  $\rho \propto r^{-2}$  everywhere. The dust-to-gas ratio is constant with value 0.01.

Model 2 uses the same parameters as used in the model for the Red Rectangle by Men'shchikov *et al.* (2002), where the model SED fits the observed continuum underlying the emission features perfectly (after considering the interstellar extinction). In model 2, the axially-symmetric dust shell has minimum radius of 14AU and maximum radius of  $r_{\text{max}} = 43,000\text{AU}$ , where 99% of the circumstellar total mass is contained within the dense torus, with maximum radius  $r_1 = 100\text{AU}$  and density with a Gaussian profile (same notation as in equation 3.48). In the torus, the dust grains have constant radius of  $a = 0.2\text{cm}$  and the dust is 100% amorphous carbon with dust-to-gas ratio  $\frac{\rho_d}{\rho} = 0.01$ . Outside this dense region, and for  $100\text{AU} = r_1 < r < r_2 = 430\text{AU}$  (equation 3.48), the dust density drops by 5 orders of magnitudes at  $r = r_1 = 100\text{AU}$  and it changes to a much flatter  $\rho \propto r^{-1.5}$  radial profile. For  $r > r_2 = 430\text{AU}$ , the density changes to  $\rho \propto r^{-4}$  to the limits of the dusty envelope at 43,000AU. Everywhere outside the dense torus, the dust-to-gas ratio is set to 0.004, the chemical composition of the dust is the same as in the torus (Hanner, 1988, 100% amorphous carbon) but the grain size distribution is the standard  $\frac{dn}{da} = a^{-3.5}$ , for  $0.005\text{μm} = a_{\text{min}} < a < a_{\text{max}} = 600\text{μm}$ . The torus and the outer parts of the envelope only exist outside the walls of a biconical cavity, with a (total) opening angle of 50 degrees and total constant density of  $\rho = \rho_3 = 9 \times 10^{19}\text{g cm}^{-3}$  for  $z < r_3$  and  $\rho \propto r^{-5}$  for  $z > r_3$ .

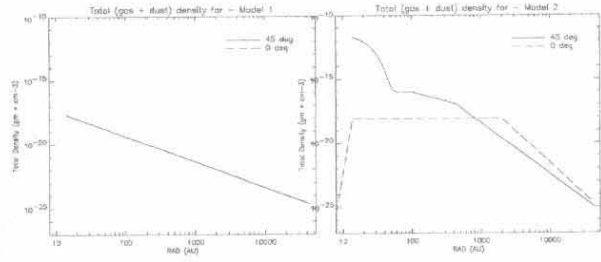


Figure 4.6: Density profile in the midplane (45 degrees) and in the bipolar outflow cavities along the symmetry axis (0 degrees), for model 1 (left) and for model 2 (Right).

The density function of model 1 and model 2 are plotted in figure 4.6. For model 1, the density follows the same profile throughout the envelope and the density curve for the bipolar cavities (0 degrees) has values too low to appear within the range plotted.

The density in model 2 (figure 4.6) follows a Gaussian profile in the very dense torus, centred at the origin of the coordinate system with standard deviation  $\sigma = 11\text{AU}$ . We have modified CSRE to use this density structure to reproduce the density used in Men'shchikov *et al.* (2002).

The best model fit for model 1 is the total model SED without interstellar extinction (blue dotted line, figure 4.7), however this is not a good fit to all the observational data.

To get a better fit to the observations using our model of the Red Rectangle with the same density structure as Men'shchikov *et al.* (2002) (figure 4.6), the interstellar extinction must be taken into account, i.e. the solid pink line is a better fit than the blue dotted line in figure 4.8. The value for the IS extinction used in our model,  $A_V = 1$  is consistent with the value used in Men'shchikov *et al.* (2002) of  $A_V = 0.9$ . This is due to the fact that we are using the same kurucz input profile, the same density and the same geometry for our model. In both figures 4.7 and 4.8, the IS extinction is not important for wavelengths larger than  $3\text{μm}$ , i.e. the blue dotted and the solid pink lines are identical.

Using this density profile and geometry parameters, and assuming that when one would fit the SED for longer wavelengths the fit in the UV and optical part of the spectrum would not be destroyed, then, the estimate of a distance of 710 pc ( $A_V = 1$  corresponds to a distance to the object of  $\sim 710\text{pc}$ , Men'shchikov *et al.*, 2002) to the object is a valid conclusion from our modelling because a good fit to the UV and optical observations is only obtained considering IS extinction.

Assuming a relationship between  $A_V$  and the distance in the ISM along a line of sight close to the RR, then an extinction correction of  $A_V \sim 1$  corresponds to a distance of 710 pc.

Table 4.1: Model parameters for two alternative models of the Red Rectangle

Model 1		Model 2 <sup>a</sup>	
Parameter	Value	Parameter	Value
Central Source Properties		Central Source Properties	
$R_*$ ( $R_\odot$ )	43	$R_*$ ( $R_\odot$ )	43
$T_\odot$ (K)	7,750	$T_\odot$ (K)	7,750
Envelope Properties		Envelope Properties	
$r_{\max}$ (AU)	43,000	$r_{\max}$ (AU)	43,000
$r_{\min}$ (AU)	14	$r_{\min}$ (AU)	14
CHOIE	YES	CHOIE	YES
$\theta$ (degrees) (equation 3.45)	25	$\theta$ (degrees) (equation 3.45)	25
$\beta$ (equation 3.45)	1	$\beta$ (equation 3.45)	1
$z_0$	0 (equation 3.45)	$z_0$	0 (equation 3.45)
Density Parameters		Density Parameters	
$\rho_{\text{amb}}$ ( $\text{g cm}^{-3}$ )	0.0	$\rho_{\text{amb}}$ ( $\text{g cm}^{-3}$ )	0.0
$\rho_0$ ( $\text{g cm}^{-3}$ ) (equation 3.44)	$1.0 \times 10^{-14}$	$\rho_1^I$ ( $\text{g cm}^{-3}$ ) (equation 3.48)	$4.2 \times 10^{-12}$
$\alpha$ (equation 3.44)	2	$\rho_1^{II}$ ( $\text{g cm}^{-3}$ ) (equation 3.48)	$1.0 \times 10^{-15}$
$f$ (equation 3.44)	0	$\rho_2^I$ ( $\text{g cm}^{-3}$ ) (equation 3.48)	$1.0 \times 10^{-16}$
$\rho_{\text{cavity}}$ ( $\text{g cm}^{-3}$ ) (equation 3.46)	$0.0 \times 10^{-20}$	$\rho_2^{II}$ ( $\text{g cm}^{-3}$ ) (equation 3.48)	$1.2 \times 10^{-17}$
$\gamma$ (equation 3.46)	2	$\rho_3$ ( $\text{g cm}^{-3}$ ) (equation 3.48)	$9.0 \times 10^{-19}$
Dust Parameters		Dust Parameters	
$q$ (table 3.3)	3.5	$q^b$ (table 3.3)	3.5
$a_{\min}$ ( $\mu\text{m}$ ) (table 3.3)	0.005	$a_{\min}$ ( $\mu\text{m}$ ) <sup>c</sup> (table 3.3)	0.005
$a_{\max}$ ( $\mu\text{m}$ ) (table 3.3)	600.0	$a_{\max}$ ( $\mu\text{m}$ ) <sup>d</sup> (table 3.3)	600.0
		$a_0$ (cm) <sup>e</sup>	0.2
		AFLAG	1 thus $a = \frac{Q_{\text{ext}}}{Q_{\text{ext}}}$
		GFLAG	1 thus anisotropic scattering
		KFLAG	0 thus $k = 0.4 \times k_{\text{dustfile}}$
Output Data		Output Data	
$\Theta$ (degrees)	79 <sup>f</sup>	$\Theta$ (degrees)	79

<sup>a</sup>using CSRE after the modifications described in section 3.5, page 40

<sup>b</sup>outside the torus

<sup>c</sup>outside the torus

<sup>d</sup>outside the torus

<sup>e</sup>constant grain size in the torus

<sup>f</sup>equivalent to a 11 degrees viewing angle

#### 4.3.2 Same $A_V$ , different density

The aim of model 3 is to have the same optical depth along the equator (through the torus) as in Men'shchikov *et al.* (2002). To obtain such a high  $A_V$  of  $\sim 42$ , model 3 has the same input parameters as model 2 (listed in table 4.1) but the torus density Gaussian profile is defined by a larger value of  $\rho_1^I$  given by  $\rho_1^I = 3.0 \times 10^{-11} \text{ g cm}^{-3}$ .

Model 3 is a worse fit to the observations than models 1 and 2. The thermal emission dominates the SED at longer wavelengths ( $\lambda \geq 3 \mu\text{m}$ ) and the fit with model 3 in this region is similar to the fit obtained with models 1 and 2, but in the UV and optical parts of the spectrum, the fit is completely lost due to the higher optical depth.

The result is that one cannot have the same density function as used in Men'shchikov *et al.* (2002) and, simultaneously, the same values for the optical Extinction.

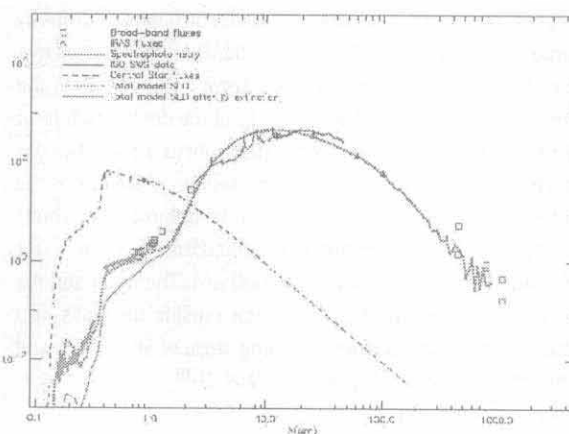


Figure 4.7: Observed SED of the Red Rectangle compared with model SED for small dust grains (model 1).

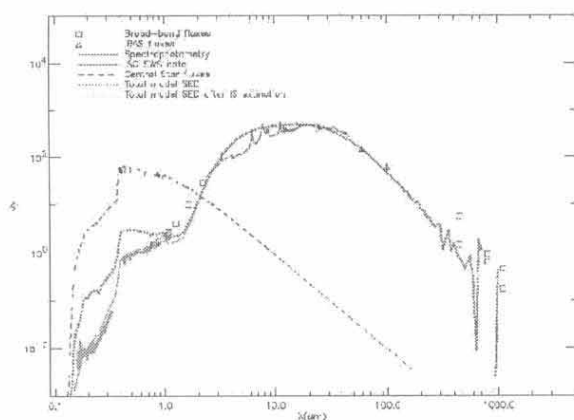


Figure 4.8: Observed SED of the Red Rectangle compared with model SED for large dust grains (model 2).

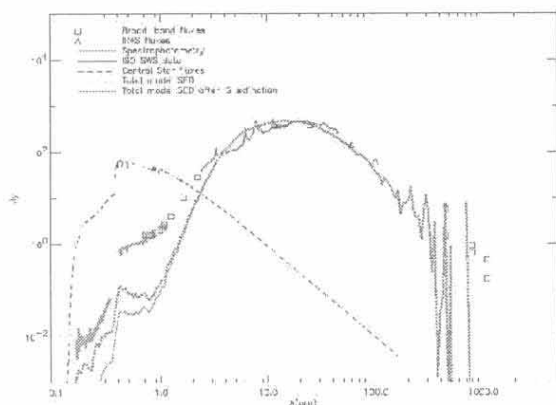


Figure 4.9: Observed SED of the Red Rectangle compared with model SED for large dust grains and  $A_V = 42$  (model 3).

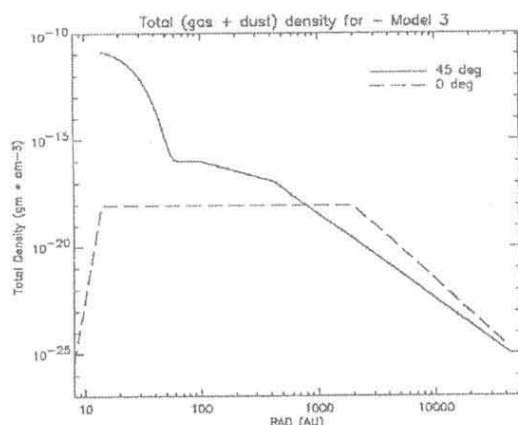


Figure 4.10: Density profile in the midplane (45 degrees) and in the bipolar outflow cavities along the symmetry axis (0 degrees), for model 3.

#### 4.4 Discussion

Model 1 and model 2 are not satisfactory fits to the observations, however, it is possible to conclude some results from our modelling.

Based on the results obtained by using both versions of CSRE, it is not possible to say that the use of large grains and complex density distributions (model 2) is a better description of the object compared with that of standard grains and the usual  $\rho \propto r^{-2}$  because both SEDs (figures 4.7 and 4.8) are equally good. Moreover, model 1 does not require any IS extinction to reproduce the observations with the same degree of accuracy as model 2.

Compared to the successful model presented by Men'shchikov *et al.* (2002), our model 2 is an identical model in all but one aspect, as far as it was possible to understand from the published details. We have the same density profile (including the peculiar density function in the torus and cavities), the same variable dust-to-gas ratio, the same geometry of the circumstellar envelope, the same atmosphere input spectrum and we are comparing the model with the same observational data. But our model considers realistic dust properties and scattering modelling, throughout the envelope (including the dense torus). It is not possible to reveal from the published information, what was the chemical composition of the dust used in the torus. The information published in Men'shchikov *et al.* (2002), with respect to this point, is inconclusive but we believe that dust with an unspecified chemical composition (only characterised by a grey optical depth and constant grain size of 0.2  $\mu\text{m}$ ) was used and this is the reason why our model 2 has a much lower optical depth of  $A_V = 6.8$  along the midplane compared to  $A_V = 47$  used in Men'shchikov *et al.* (2002). It was not possible to reproduce the same  $A_V$  and the same density function with CSRE, in the same model.

The best observational constraint on the midplane extinction for the Red Rectangle is presented in Men'shchikov *et al.* (2002), using the  $H$ ,  $K$  (76 mas resolution), and  $K_s$ ,  $L_c$  (47 and 74 mas resolution, figure 4.5) nearinfrared images (published in, Men'shchikov *et al.*, 1998, 2002; Tuthill *et al.*, 2002). Its value is  $A_V = 47$  up to  $\lambda \sim 1 \mu\text{m}$ , referring to a optically thick torus. This result was our main motivation to produce model 3, described next.

Model 3 has a similar  $A_V$  ( $A_V = 42$ ) compared to the one used in the referred paper, but the density function is different, as it is possible to conclude comparing figures 4.6 where the same density profile is used in figure 4 of Men'shchikov *et al.* (2002), and figure 4.10. The conclusion is that a more similar SED is obtained when we have the same density function (figure 4.8) rather than having the same  $A_V$  (figure 4.9).

Using CSRE and realistic dust and scattering considerations, one either have the same density profile as used in Men'shchikov *et al.* (2002) but have different  $A_V$ , or have the same  $A_V$  but have a different density profile. We argue that the reason why we could not reproduce the *perfect* fit presented in the referred article is not because CSRE model is wrong or too simple, in fact, all modifications were made during this work to CSRE to reproduce the Men'shchikov *et al.* (2002) model and, crucially CSRE has been proved to be a physically valid model (in particular in the way anisotropic scattering is considered) by the discussion of the comparison results presented in section 3.6.

Therefore it is plausible to argue that some component of the Men'shchikov *et al.* (2002) model of the Red Rectangle may be too simplistic or may be based on a not very realistic assumption, e.g. perhaps the dust properties in the torus are a crude approximation to the real dust properties. This may be the reason why his model fits the continuum data perfectly.

## 5 - Conclusion

This Chapter summarises the work done during this MSc by Research dissertation and gives the conclusions of it. Also discussed is possible future work.

### 5.1 Summary

Chapter 2 gives a review of the standard theory of stellar evolution after the main sequence, with focus on the post-AGB phase and the dual-chemistry sources.

The fundamental equations of the radiative transfer and temperature equilibrium in a dusty medium were presented (chapter 3) and two radiative equilibrium computer codes were presented (DART and CSRE) that implemented the monte carlo and the ray-tracing methods, respectively. In the monte-carlo method individual photons are followed throughout their random walk until they finally escape generating an energy distribution in wavelength (SED) and images. In the ray-tracing method the radiative transfer equation is solved at each point of the envelope.

In order to solve the radiative transfer problem and to model the dusty envelope of post-AGB stars, we have modified an existing monte-carlo radiative equilibrium code, CSRE, used for modelling young stellar objects. Dust grains are considered to be solely responsible for radiative transfer in these systems. It is therefore crucial to be able to generate realistic dust grains properties. These were computed from laboratory measured refractive indices of different dust types and used as an input for CSRE.

In Chapter 4, a discussion based on three possible models for the Red Rectangle, and comparing with a published model, is

presented. A critical assessment of the limitations of all models is made.

### 5.2 Conclusions

In addition to the development of crucial research skills by the author of this dissertation during the past 12 months, the interesting results emerging from this work are listed below:

- CSRE (in any of its versions) is a sophisticated and valid radiative transfer code that is now well suited to model post-AGB stars with dual-chemistry properties and others astrophysical objects with discs or tori and sharp density contrasts. In particular, CSRE considers the scattering of electromagnetic radiation by dust grains in a physically realistic way even for systems with high optical depths ( $\tau \geq 4$ ),
- DART code (and any other code that assumes isotropic scattering) gives inaccurate results for systems with high optical depths ( $\tau \geq 4$ ), because, for low values of optical extinction the SED is dominated by the stellar direct fluxes and the average photon is scattered a small number of times, and hence, scattering is not important. A more realistic forward-scattering phase (anisotropic scattering) function will generate a higher value of scattering fluxes because, in an envelope where the density is decreasing radially, the scattered photons have a higher probability of being scattered forward towards the observer as more photons are propagated radially with anisotropic scattering than with isotropic scattering. Thus, the results of CSRE and DART will diverge and we argue that CSRE gives a physically more realistic result.
- The result of the modelling presented in Chapter 4 is inconclusive with respect to derived physical properties of the Red Rectangle because a good fit to all observational fluxes was not obtained, however,
- we argue that a set of results from our modelling of the Red Rectangle is still valid:
  - the need for millimetre size grains in the Red Rectangle is not obvious, in fact, a model using exclusively grains with standard size distribution is equally good
  - a distance of 710 pc is consistent with our model fit in the UV and optical wavelengths, however, this is dependent on the required IS correction, which depends on the dust model used. E.g., the small

grains model (model 1) does not need any IS correction

– the Men'shchikov *et al.* (2002) model of the Red Rectangle may be too simplistic or not very realistic in its treatment of scattering and dust properties in the torus (these properties are crucial for this type of high optical depth systems, as has been demonstrated during this dissertation in section 3.6) and this may be the reason why that model fits the data perfectly,  
– we argue that further investigation of other density profiles, would yield arguably good fits to the observed fluxes.

- CSRE can reproduce all the important physical quantities that are available in a ray-tracing method, such as the various intensity moments.
- the use of true random numbers generated from a chaotic source external to the deterministic computer would be an important qualitative improvement to any monte-carlo code, but in practice this is not possible due to the present computer capabilities.
- CSRE only considers dust radiative transport, and the source of opacity (the dust) must be temperature-independent. This can be a limitation, and therefore CSRE cannot be used to model temperature dependent sources of opacity such as photoionized gaseous nebulae where the opacity varies with the local temperature.

### 5.3 Future Work

Increasingly complex dust properties can now be used as an input for CSRE thus enabling the modelling of emission features such as PAH or crystalline silicates.

CSRE is a sophisticated and reliable code that can be used to model not only dual-chemistry post-AGB stars but also other astrophysical systems that have a disc or a torus, e.g. AGN or discs around Brown Dwarfs. Also, any density profile can be included in CSRE and this increases even more the range of systems that are possible to be modelled with CSRE.

With respect to post-AGB stars, CSRE can be used to model dust emission from post-AGB stars and compare them with spectra from observational data (e.g., the ISO archive) to determine whether the location of the O-rich material can be determined by fits to the observed spectral features, and hence whether the dust responsible for these features lies in a disc (or torus) close to the star or at larger distances (more consistent with the cometary hypothesis).

## A - CSRE code

CSRE follows a divide-an-conquer strategy to tackle the problem described in Section 3.1. This modular design is important for development and maintenance. The relevant theoretical results obtained in Section 3.1 will be implemented and examples of the code lines are described.

### A.1 CSRE Architecture

We choose to develop the modifications to CSRE in FORTRAN 77 chiefly because this was the programming language used in Whitney *et al.* (2003a), but also because this seems to be one of the preferred language used in astrophysics over the past years. The code runs on Sun workstations and PCs with Linux. The models takes 30 min to produce high frequency resolution and low noise spectra at all inclinations on 1 GHz Linux PC (g77 FORTRAN). To produce SEDs and high-quality images takes ~5 hours.

The next paragraphs contain concise explanation of the more important CSRE's subprograms. We define *level number*,  $\gamma$ , as a number that tells the hierarchy rank of the sub-program. E.g., the main program has level number  $\gamma = 0$  and all the sub-programs called by the main program have level number  $\gamma = 1$ , and so forth. These are in order of increasing level number.

#### A.1.1 Main Program: program tts [ $\gamma = 0$ ]

Program tts is the main program in the CSRE code. It is the only program with  $\gamma = 0$ . All other subprograms (either functions or subroutines) are controlled by this program unit.

In the *specification* part of the program tts, the type of the variables used in the program are specified and some values of variables are initialised.

The first lines in the execution part are used to open the disk.dat and RANDOM.dat. All the subroutines used in CSRE write information, variables values and warning messages, in the disk.dat file. The RANDOM.dat file simply registers the value of the variable JRANC, which is the number of times the random number generator is used during the CSRE code in a specific run.

Then 6 subroutines are called: *setup* - problem setup and parameter input, *dustinit* - input of dust parameters, *atmosinit* - reads in a two-column array containing wavelengths and fluxes associated with the the central source *initarr* - initialise the arrays variables to be used, *disk* - Monte Carlo Radiative Transfer subroutine, and *output* - write output files.



### A.1.2 program setup [ $\gamma = 1$ ]

Program setup is the subroutine responsible for the reading in the input values for the variables to be used in the code.

In the *specification part* of the program, the type of the variables used in the program are specified and some values of variables are initialised.

In the *execution part*, the  $\gamma = 2$  subroutine `reapar` is used to read in the values present in the input file. These include the file names for the atmosphere spectrum of central source, dust files and the values for the parameters used. These are described in table 3.1.

### A.1.3 program dustinit [ $\gamma = 1$ ]

Program `dustinit` is the subroutine responsible for the reading in the input values for the variables from the dust files to be used in the code and for initialising the values relative to the Radiative Equilibrium Temperature, e.g. Pre-tabulate the values for the Planck mean opacity,  $k_p$ , for a large range of temperatures. This table will be then used to find the temperature from heating by the cumulative photon absorption.

CSRE accepts 3 dust files. One file for each region of the circumstellar nebula. A dust file is a table with 5 columns and each line corresponding to a value of wavelength. Every column  $i$ ,  $i = 0, 4$  (refer to table 3.3) is a physical quantity obtained using Mie Theory (Section 3.5.1):  $i = 0 \rightarrow$  wavelength,  $i = 1 \rightarrow$  extinction cross section,  $i = 2 \rightarrow$  scattering cross section,  $i = 3 \rightarrow$  opacity,  $i = 4 \rightarrow$  scattering asymmetry parameter.

These files are generated before CSRE is run. The program `dustprop` is used to apply Mie Theory and generate these physical quantities ( $i = 0, 4$ ), specific for each dust grain population. A grain population is defined by the input parameters described in table 3.3.

It is in `dustinit` that the input flag parameters AFLAG, GFLAG and KFLAG (table 3.1) are used in CSRE. A set of simple IF cycles are used to choose between the two options for each flag. The scattering asymmetric parameter  $g$  (FORTRAN variable `gdust`) can be forced to have the value  $g = 0$  if isotropic scattering is assumed

for that specific model. Then, the GFLAG determines whether this value for  $g$  is used or  $g$  is read from the dust file (FORTRAN variable `hgg`):

```
IF (GFLAG.EQ.0) THEN
    gdust(i,id) = 0
ELSE
    gdust(i,id) = hgg
ENDIF
```

A similar code is implement with respect to AFLAG and KFLAG.

This subroutine is also responsible for calculating the average value for the optical depth in each dust region. This is saved into an array with dimension 3, i.e. it has the value for the average optical depth for each dust properties. These average values are used in section A.1.6, when the optical depth along every  $\theta$  direction is calculated.

### A.1.4 program atmosinit [ $\gamma = 1$ ]

Program `atmosinit` is the subroutine responsible for the reading the wavelengths and fluxes of the central source spectrum. The subroutine expects the input file (ATNAME, table 3.1) to be present before CSRE is run.

The central source spectrum can be a blackbody curve or any other model atmosphere spectra. Two FORTRAN programs have been prepare to generate a file with the correct format to be used as CSRE input file from blackbody spectrum at a specific chosen temperature and a downloaded atmospheric model from Kurucz (1993), parameterised by the effective temperature  $T_{\text{eff}}$ , gravity  $g$ , metalicity and micro-turbulent velocity.

### A.1.5 program initarr [ $\gamma = 1$ ]

Program `initarr` is the subroutine in charge of initialising the arrays variables used during a CSRE run. Initializing an array consist in defining its type, dimension and setting all the entries to zero.

### A.1.6 program disc [ $\gamma = 1$ ]

The core of CSRE is in the program `disc`. It is here that the Monte Carlo method for Radiative transfer and Temperature correction discussed in Chapter 3, section 3.4 is implemented.

In the *specification part* of the program, the type of the variables used in the program are specified and some values of variables are initialised. It is here that, for the first time in CSRE that the FORTRAN variable `ran2` is defined. This variable is crucial because it stores the random values used in the probabilistic nature of the monte carlo code. Every time this variable is used in CSRE it is highlighted in this section.

The  $\gamma = 2$  subroutine `gridset` is used in the program `disc` to set up the 3D density function. The density function is defined in a 3D grid under spherical coordinates  $(r, \theta, \phi)$ , i.e. the envelope is divided into  $n_r$  cells in the  $r$  dimension,  $n_\theta$  in the  $\theta$  dimension and  $n_\phi$  along the  $\phi$  dimension. The density is set to be constant within each  $j$  grid  $(r_j, \theta_j, \phi_j)$ . Numerically this is done using 3 nested DO ... END DO cycles.



```

DO IR=1, NRG-1
RAD = ravearr(IR)

DO IT=1, NTG-1
THETA= thetarr(IT)

DO IP=1, NPG-1
PHI = phiarr(IP)

CALLDENSENV(rad,thet, cost,sint,pi, 1 pihalf,
phi, DENSE,radamb, IDE)

DUSTARR(ir,it,ip)= IDE
END DO
END DO
END DO

```

The FORTRAN variables IR, IT and IP, represent the index values of the ravearr, thetarr and phiarr,  $r$ ,  $\theta$  and  $\phi$  arrays (defined in the subroutine initarr), respectively. These have integer values in the range defined from 1 to the maximum number of cells in each dimension, NRG, NTG and NPG. Basically, this is how CSRE assigns a constant value for the density within each grid cell.

To do this, the  $\gamma = 3$  subroutine DENSENV is used to calculate a value for the density function for the  $IR = i$ ,  $IT = j$ ,  $IP = k$  cell. The density function defined in DENSENV depends on where in the envelope the point with coordinates  $(r, \theta, \phi) = (\text{ravearr}(i), \text{thetarr}(j), \text{phiarr}(k))$  is. This selection is done using nested IF ... END IF clauses.

For region 1 and 2:

```

c Region 1 (Torus):
IF (RAD.LT.(JRMX1 * RMAX).AND.RAD.GT.RMINE)
THEN
  DENS = ((RHOC1R1 - RHOC2R1) *
$ (EXP(-(((RAD - MU1) ** 2)/(2 * (SIGMA1**2))))))
$ + RHOC2R1
  IDUST2 = 1
ELSE
  c Region 2:
  IF (RAD.LT.(JRMX2 * RMAX).AND.RAD.GT.JRMX1*
RMAX) THEN
    DENS = CONST2A * RHOC1R2 * (RAD ** (-EXP1R2))
    IDUST2 = 2
  ELSE
    IF (RAD.LT.RMAX.AND.RAD.GT.(JRMX2 * RMAX))
    THEN
      DENS = CONST2B * RHOC2R2 * (RAD ** (-EXP2R2))
      IDUST2 = 2
    
```

```
ELSE
```

```
DENS = 0.
```

```
ENDIF
```

```
ENDIF
```

```
ENDIF
```

Region 1 is a spherical shell defined by its minimum and maximum radius, RMINE and JRMX1. These are the user-defined input parameters (described in table 3.1),  $r_{\min}$  and  $r_1$ , respectively. The density function here has a Gaussian profile fixed by its value at  $r = \mu$  and at  $r_1$ , and by the Gaussian mean value and standard deviation. These are predetermined by the user in the input values of  $\rho_1^I$  and  $\rho_1^{II}$ ,  $\mu$  and  $\sigma$ , in the same order (described in table 3.1).

Region 2 is a spherical shell defined by its minimum, maximum radius and by its characteristic radius, JRMX1, RMAX and JRMX3. These are the user-defined input parameters,  $r_1$ ,  $r_{\max}$  and  $r_2$ . The density function here follows a power law over reestablished by its value at  $r_1$  and by a power-law exponent, for  $r < r_2$ , and by its value at  $r_2$  and by a power-law exponent, for  $r_2 < r < r_{\max}$ . These are predetermined by the user in the input values of  $\rho_2^I$  and  $\beta I$ ,  $\rho_2^{II}$  and  $\beta II$ , respectively.

If CHOLE is set to YES, then a bipolar cavity is carved out of the envelope structure described by regions 1 and 2. The polar cavities region is defined as region 3. This region is adjusted by three parameters,  $\theta$ ,  $\alpha$  and  $z_0$ . These are the opening angle, the wall exponent and the height of cavity wall at the origin, respectively. A conical cavity with vertices at  $r = 0$  ( $\Leftrightarrow x = y = z = 0$ ) is obtained setting  $\alpha = 1$  and  $z_0 = 0$ , but a more general cavity is created for different values of these parameters. The equation implemented in the code that shape the cavity is equation A.1,

$$Z = z_0 + \Xi \varpi^\alpha \quad (\text{A.1})$$

where,  $Z$  is the  $z$  coordinate of a point that is located in the cavity wall,  $\varpi = \sqrt{x^2 + y^2}$  is the cylindrical radius and  $\Xi = f(\theta)$  is a function  $f$  of the opening angle,  $\theta$ .

The points belong to the cavity if  $z > Z$ . In the code,  $Z$  is represented by ZUP and the characteristic radius  $r_3$  is JRMX3. The density function in the polar cavity is a constant function for  $r < r_3$  and has a power-law profile for  $r > r_3$ . The constant part of the density function is set by the input parameter  $\rho_3$ , and in the power-law part the density is  $\alpha \rho_3^\gamma$ . Thus, for region 3:

```
IF (ZP.LT.(JRMX3 * RMAX).AND.ZP.GT.ZUP) THEN
```

```
DENS = RHOC1R3
```

```

IDUST2 = 3

ELSE

Region B:

IF (ZP.GT.(JRMX3 * RMAX).AND.ZP.GT.ZUP) THEN

    DENS = CONST3 * RHOC1R3 * (RAD ** (-EXPR3))
    IDUST2 = 3

ENDIF
ENDIF
ENDIF

```

All the above code lines can be encapsulate in the equation 3.48 and are represented in figures 3.6 and 3.7.

The density function  $\rho(r)$  (FORTRAN variable DENS) is written as a function of the position vector  $r = (r, \theta, \phi)$  because regions 1 and 2 are defined in spherical co-ordinates but region 3 is defined in normal Cartesian co-ordinates.

The parameters  $A, B$  and  $C$  are the FORTRAN variables CONST2A, CONST2B and CONST3. These are normalisation constants with values of  $A = r_1^{\beta_1}$ ,  $B = r_2^{\beta_2}$  and  $C = r_3^{\gamma}$ .

All other parameters present in equation 3.48 are described in table 3.1.

It is clear in this equation that the division in regions 1, 2 and 3 is a division with respect to the dust type in each region. It is possible to have different densities profiles within the same region but it is not possible to have different dust properties within the same region.

This division is implemented by the variable IDUST2. This variable is set to 1, 2 or 3 inside the  $\gamma = 3$  subroutine DENSENV and its value is passed to the  $\gamma = 2$  subroutine gridset. Here, an 3D array is filled with the index corresponding to each region. The array is DUSTARR and to allocate its values correctly it must be inside the 3 nested DO ... END DO cycles explained above. Therefore, if the point in the envelope defined by  $IR = i, IT = j, IP = k, (r, \theta, \phi) = (r_{\text{earr}}(i), \theta_{\text{earr}}(j), \phi_{\text{earr}}(k))$ , belongs to region  $n, n = 1, 2, 3$  then  $DUSTARR(i, j, k) = n$ .

It is clear from the discussion present in Chapter 3, that the optical depth is the key parameter that determines the distance between interactions. At this point, the CSRE core has all the values needed to calculate the optical depth. These are the density, and the value of the opacity in every point (i.e. grid cell) of the envelope. The opacity is an input to CSRE and its values are read in the  $\gamma = 1$  subroutine dustinit.

To calculate the average optical depth along every  $\theta$  direction,  $\tau$ , the integral equation 3.27 (deduced in Chapter 3) must be calculated for every path of constant  $\theta$ . The integral is not solve analytically but numerically. The integral is approximate to the sum of individual rectangles with area  $A = (k\rho) \Delta r$ , i.e.,

$$\bar{\tau} \approx \sum_r (k\rho) \Delta r \approx \bar{k} \sum_{i_r} \rho_{i_r} \Delta r \quad (\text{A.2})$$

where  $\Delta r = r_{i_r+1} - r_{i_r}$  and  $\bar{k}$  is the average optical depth for each dust region (calculated in section A.1.4).

Equation A.2 was solved using the following FORTRAN code lines:

```

do it=1,ntg-1
do ir=1,nrg-1
    Dr=rarr(ir+1)-rarr(ir)

    Call densenv(rad,thet,cost,sint,pi,
1          pihalf,phi,dense, radamb,ide)

    Id=dustarr(ir,it,1)

    Tauc=tauc+kapd(id)*(dense)*dr

end do

Tauave=tauave+tauc

end do

```

where  $\Sigma_{ir}$  is the DO ... END DO loop in combination with  $\text{tauc} = \text{tauc} + \text{kapd}(id) * (\text{dense}) * dr$ ,  $\Delta r$  is  $dr$ ,  $\rho_{ir}$  is  $\text{dense}$  and  $\bar{k}$  corresponds to  $\text{kapd}(id)$ . The FORTRAN variable  $\text{tauc}$  is the optical depth at a specific angle. (and this is printed to a file), and  $\text{tauave}$  is the  $\theta$  average optical depth. From the values of  $\text{tauc}$ , and using directly equation A.3 one can promptly tabulate the values of the visual extinction (V band 5,500Å) measured from the star through the envelope, at all  $\theta$  angles, using equation A.3,

$$A_V = \tau 2.5 \log_{10} e \approx 1.086 \tau \quad (\text{A.3})$$

In the code,  $AV = 1.086 * \text{tauc}$ .

The density grid and the dust regions are now ready for the moment when the photons will be emitted! But before that, the  $\gamma = 2$  subroutine filt is used to define the image filters. These are very practical to compare the results from the CSRE modelling with real observations. filt simply reads in the instrumental response of a desired filter installed e.g. at HST NICMOS from a filter file, and this is then used when CSRE creates images of the system modelled. There are some filter files built-in, these are HST NICMOS near-Infrared and Spitzer IRAC and MIPS. But the user can use other filters files.

The *central part* of the execution part is the loop over stellar photons. It is in this loop that the sequence: *a photon is emitted, it travels a distance, and something happens to it*, is numerically implemented, until all photons escape the circumstellar envelope (see figure 3.1). The radiation transfer technique is described in Chapter 3. The basic idea is to divide the luminosity of the radiation from the central source into equal-energy, monochromatic (i.e. with one determined value of frequency) photons that are emitted by the source. These photons travel a distance  $L$ , determined by the optical depth, where they are either scattered or absorbed with a probability given by the albedo. If the random number RAN2 decides that the photon is scattered, then a random scattering angle is obtained from the scattering phase function and the photon continues to a new interaction place. If instead the photon is absorbed, its energy is added to the envelope, raising the local temperature. To conserve energy the photon is reemitted at a new frequency. These reemitted photons are the diffuse radiation field. This is where most of the execution time is spent during CSRE run.

### Bibliography

- ALLAMANDOLA, L., CAMI, J., COHEN, M., MARWICK-KEMPER, C. & VAN WINCKEL, H. (2006). The Red Rectangle: Meeting. Web Site: [www.theredrectangle.net](http://www.theredrectangle.net).
- ALLEN, D.A., HYLAND, A.R., LONGMORE, A.J., CASWELL, J.L., GOSS, W.M. & HAYNES, R.F. (1977). Optical, infrared, and radio studies of AFGL sources. *Astrophysical Journal*, **217**, 108–111.
- BALICK, B. (2002). Shapes and shaping of planetary nebulae. *Annual Review of Astronomy and Astrophysics*, **40**, 439–486.
- BJORKMAN, J.E. & WOOD, K. (2001). Radiative equilibrium and temperature correction in monte carlo radiation transfer. *The Astrophysical Journal*, **554**, 615–623.
- BLÖCKER, T. (1995a). Stellar evolution of low and intermediate-mass stars. I mass loss on the AGB and its consequences for stellar evolution. *Astronomy & Astrophysics*, **297**, 727.
- BLÖCKER, T. (1995b). Stellar evolution of low and intermediate-mass stars. II post-AGB evolution. *Astronomy & Astrophysics*, **299**, 755.
- BLÖCKER, T. (2001). Evolution on the AGB and beyond: on the formation of H-deficient post-AGB stars. *Astrophysics and Space Science*, 1–14.
- BOHREN, C.F. & HUFFMAN, D.R. (1983). *Absorption and scattering of light by small particles*. Wiley.
- BOWEN, G.H. (1988). Dynamical modelling of long-period variable star atmosphere. *Astrophysical Journal*, **329**, 299–317.
- CARROL, B.W. & OSTIE, D.A. (1996). *An Introduction to Modern Astrophysics*. Addison-Wesley Publishing Company, Inc.
- COHEN, M., ANDERSON, C.M., COWLEY, A., COYNE, G.V., FAWLEY, W., GULL, T.R., HARLAN, E.A., HERBIG, G.H., HOLDEN, F., HUDSON, H.S., JAKOUBEK, R.O., JOHNSON, H.M., MERRIL, K.M., SCHIFFER, F.H., SOIFER, B.T. & ZUCKERMAN, B. (1975). The peculiar object - the Red Rectangle. *Astrophysical Journal*, **196**, 179–189.
- COHEN, M., BARLOW, M., SYLVESTER, R., LIU, X., COX, P., LIM, T., SCHMITT, B. & SPECK, A. (1999). Water ice, silicate, and polycyclic aromatic hydrocarbon emission features in the infrared space observatory spectrum of the carbon-rich planetary nebula CPD -56 deg 8032. *The Astrophysical Journal*, **513**, L135–L138.
- COHEN, M., VAN WINCKEL, H., BOND, H. & GULL, T. (2004). Hubble space telescope imaging of the HD44179, the Red Rectangle. *The Astronomical Journal*, **127**, 2362–2377.
- DE RUYTER, S., VAN WINCKEL, H., DOMINIK, C., WATERS, L.B. & DEJONGHE, H. (2005). Strong dust processing in circumstellar discs around 6 RV Tauri stars. Are dusty RV Tauri stars all binaries? *Astronomy & Astrophysics*, **435**, 161–166.
- DRAINE, B.T. & LEE, H.M. (1984). Optical properties of interstellar graphite and silicate grains. *Astrophysical Journal*, **285**, 89–108.
- EFSTATHIOU, A. & ROWAN-ROBINSON, M. (1990). Radiative transfer in axisymmetric dust clouds. *Monthly Notices Royal Astronomical Society*, **245**, 275–288.
- ENGELS, D. (2005). AGB and post-AGB stars. *Astro-ph*, **0508285**.
- ERCOLANO, B. (2002). *Three Dimensional Monte Carlo Simulations of Ionised Nebulae*. Ph.D. thesis, University College London, London, UK.
- FORREST, W.J., HOUEK, J.R. & MCCARTHY, J.F. (1981). A far-infrared emission feature in carbon-rich stars and planetary nebulae. *Astrophysical Journal*, **248**, 195–200.
- GARCIA-LARIO, P. & CALDERON, J.V.P. (2003). The transition from AGB stars to planetary nebulae as seen by ISO. *ESA Publications Series, Exploiting the ISO Data Archive*, 97.
- GILRA, D.P. (1973). Dust particles and molecules in the extended atmospheres of carbon stars. *Interstellar Dust and Related Topics, IAU Symposium no. 52*, 52.
- GLEDHILL, T.M. & YATES, J.A. (2003). Mid-infrared imaging of the dust shell around the post-asymptotic giant branch star HD 161796. *Mon. Not. R. Astronomy Soc.*, **343**, 880–890.
- GREAVES, J. & HOLLAND, W. (1997). High mass-loss carbon stars and the evolution of the local  $^{12}\text{C}/^{13}\text{C}$  ratio. *Astronomy & Astrophysics*, **327**.
- HAAHR, M. (2005). Random.org. Web site: [www.random.org](http://www.random.org).
- HANNER, M. (1988). Grain optical properties. *NASA Conf. Pub.*, **3004**, 22–49.
- HERWIG, F. (2005). Evolution of asymptotic giant branch stars. *Annual Review of Astronomy and Astrophysics*, **43**, 435–479.
- HOOGZAAD, S.N., MOLSTER, F.J., DOMINIK, C., WATERS, L.B.F.M., BARLOW, M.J. & KOTER, A. (2002). The circumstellar dust shell of the post-AGB star HD161796. *Astronomy & Astrophysics*, **389**, 547–555.
- JURA, M., TURNER, J. & BALM, S.P. (1997). Big grains in the Red Rectangle. *Astrophysical Journal*, **474**, 741.
- KURUCZ, R.L. (1993). Web site: [kurucz.harvard.edu](http://kurucz.harvard.edu).
- KWOK, S. (1975). Radiation pressure on grains as a mechanism for mass loss in red giants. *Astrophysical Journal*, **198**, 583–591.
- KWOK, S. (2000). *The Origin and Evolution of Planetary Nebulae*. 31,

Cambridge University Press.

- KWOK, S., VOLK, K.M. & HRIVNAK, B. (1989). A 21 micron emission feature in four proto-planetary nebulae. *Astrophysical Journal*, **345**, L51–L54.
- LITTLE-MARENIN, I. (1986). Carbon stars with silicate dust in their circumstellar shells. *Astrophysical Journal*, **307**, 15–19.
- MEN'SHCHIKOV, A.B., BALEGA, Y.Y., OSTERBART, R. & WEIGELT, G. (1998). High-resolution bispectrum speckle interferometry and two-dimensional radiative transfer modelling of the Red Rectangle. *New Astronomy*, **3**, 601–617.
- MEN'SHCHIKOV, A.B., SCHERTL, D., TUTHILL, P., WEIGELT, G. & YUNGELSON, L.R. (2002). Properties of the close binary and circumbinary torus of the Red Rectangle. *Astronomy & Astrophysics*.
- MOLSTER, F.J., YAMAMURA, I., WATERS, L.B.F.M., TIELENS, A., GRAAUW, T., JONG, T., KOTER, A., MALFAIT, K., ANCKER, M., VAN WINCKEL, H., VOORS, R. & WAELEKENS, C. (1999). Low-temperature crystallisation of silicate dust in circumstellar disks. *Nature*, **401**.
- MOLSTER, F.J., YAMAMURA, I., WATERS, L., L., N. & KAUF, H. (2001). IRAS 09425-6040: A carbon star surrounded by highly crystalline silicate dust. *Astronomy & Astrophysics*, **366**, 923–929.
- MOLSTER, F.J., WATERS, L.B.F.M. & TIELENS, A.G.G.M. (2002). Crystalline silicate dust around evolved stars. II the crystalline silicate complexes. *Astronomy & Astrophysics*, **382**, 222–240.
- NETZER, N. & ELITZUR, M. (1993). The dynamics of stellar outflows dominated by interactions of dust and radiation. *Astrophysical Journal*, **410**, 701–713.
- NOLL, L.C. & COOPER, S. (2005). Lavarnd. Web site: www.lavarnd.org.
- OSSENKOPF, V., HENNING, T. & MATHIS, J. (1992). Constraints on cosmic silicates. *Astronomy & Astrophysics*, **261**, 567–578.
- PACZYŃSKI, B. (1970). Stellar evolution from main sequence to white dwarf or carbon ignition. *Acta Astronomica*, **20**, 47–58.
- PEGOURIE, B. (1988). Optical properties of alpha silicon carbide. *Astronomy & Astrophysics*, **194**, 335–339.
- PRICE, S.D. & WALKER, R.G. (1976). The AFGL four colour infrared sky survey: Catalog of observations at 4.2, 11.0, 19.8 and 27.4 micrometers. *Interim Report Air Force Geophysics Lab*.
- REESE, M.D. & SITKO, M.L. (1996). Ultraviolet and visible spectropolarimetry of the Red Rectangle and HD 44179. *Astrophysical Journal Letters*, **467**, 105.
- ROWAN-ROBINSON, M. (1980). Radiative transfer in dust clouds. i. Hot-centered clouds associated with regions of massive star formation. *The Astrophysical Journal Supplement Series*, **44**, 40–426.
- SCHÖNBERNER, D. (1983). Late stages of stellar evolution II - mass loss and the transitions of the asymptotic giant branch star into hot remnants. *Astrophysical Journal*, **272**, 708–714.
- SOKER, N. (2002). Formation of double rings around evolved stars. *The Astrophysical Journal*, **577**, 839–844.
- SOKER, N. (2005). The shaping of the Red Rectangle proto-planetary nebula. *The Astronomical Journal*, **129**, 947–953.
- TIELENS, A.G.G.M. (1983). Stationary flows in the circumstellar envelopes of M giants. *Astrophysical Journal*, **271**, 702–716.
- TRAMS, N., WATERS, L., LAMERS, H., WAELEKENS, C., GEBALLE, T. & THE, P. (1991). Post AGB candidates - Selection and IR properties. *Astronomy & Astrophysics Supplement Series*, **87**, 391–382.
- TUTHILL, P.G., MENSCHIKOV, A.B., SCHERTL, MONNIER, J.D., DANCHI, W.C. & WEIGELT, G. (2002). Bispectrum speckle interferometry of the Red Rectangle: Diffraction-limited near-infrared images reconstructed from Keck telescope speckle data. *Astronomy & Astrophysics*, **389**, 889–895.
- UETA, T. (2002). *Circumstellar Distribution of Dust Grains Around Proto-Planetary Nebulae*. Ph.D. thesis, University of Illinois, Urbana-Champaign.
- VAN DER VEEN, W., WATERS, L., TRAMS, N. & MATTHEWS, H. (1994). A study of dust shells around high latitude supergiants. *Astronomy & Astrophysics*, **285**.
- VAN WINCKEL, H. (2003). Post-AGB stars. *Annual Review of Astronomy & Astrophysics*, **41**, 391–427.
- VAN WINCKEL, H. (2004). Binary post-AGB stars. *Memorie della Societa Astronomica Italiana*, **75**, 766.
- VASSILIADIS, E. & WOOD, P.R. (1994). Post-asymptotic giant branch evolution of low- to intermediate-mass stars. *The Astrophysical Journal Supplement Series*, **92**, 125–144.
- WARD-THOMPSON, D. (2005). Astro-chemistry from laboratory to telescope.
- WATERS, L.B.F.M. (2004). Dust in evolved stars. *Astrophysics of Dust - ASP Conference Series*, **309**, 229–244.
- WATERS, L.B.F.M., MOLSTER, F.J., JONG, T., BEINTEMA, D., WAELEKENS, C., BOOGERT, A., BOXHOOM, D., GRAAUW, T., DRAPATZ, S. & 28 (1996). Mineralogy of oxygen-rich dust shells. *Astronomy & Astrophysics*, **315**, 361–364.
- WATERS, L.B.F.M., WAELEKENS, C., VAN WINCKEL, H., MOLSTER, F.J., TIELENS, A.G.G.M., VAN LOON, J.T., MORRIS, P.W., CAMI, J., BOUWMAN, J., DE KOTER, A., DE JONG, T. & GRAAUW, T. (1998). An oxygen-rich dust disk surrounding an evolved star in the Red Rectangle. *Nature*, **391**.
- WHITNEY, B.A., WOOD, K., BJORKMAN, J. & COHEN, M. (2003a). Two-dimensional radiative transfer in protostellar envelopes. II an evolutionary sequence. *The Astrophysical Journal*, **598**, 1079–1099.
- WHITNEY, B.A., WOOD, K., BJORKMAN, J. & WOLFF, M.J. (2003b). Two-dimensional radiative transfer in protostellar envelopes. I. effects of geometry on class I sources. *The Astrophysical Journal*, **591**, 1049–1063.
- WILLEMS, F.J. & JONG, T. (1986). Carbon stars with oxygen-rich circumstellar dust shells: observational evidence for the onset of the carbon star phase. *The Astrophysical Journal*, **309**, L39–L42.
- ZIJLSTRA, A., CHAPMAN, J., HEKKERT, P., LIKKEL, L., COMERON, F., NORRIS, R., MOLSTER, F. & COHEN, R. (2001). Bipolar outflows in OH/IR stars. *Monthly Notices of the Royal Astronomical Society*, **322**, 280–308.